Short Papers

A New Unequal Three-Tone Signal Method for AM–AM and AM–PM Distortion Measurements Suitable for Characterization of Satellite Communication Transmitters/Transponders

F. M. Ghannouchi, H. Wakana, and M. Tanaka

***Abstract*—A new method for characterization of AM–AM and AM–PM distortion of power amplifiers (PA's) using only power measurements is proposed in this paper. This technique was found to be suitable for the characterization of satellite communication transmitters/transponders. It consists of using an unequal three-tone signal (UTTS) to drive either the base-station PA's transmitter or the satellite transponder's PA and to measure the level of this UTTS at the output of the transmitter/transponder. By comparison of the three tone levels at the input and output of the transmitter/transponder, one can calculate the AM–AM compression factor and AM–PM conversion coefficient of the transmitter/transponder PA using close-form expressions.**

***Index Terms*—Amplitude compression, nonlinear characteristics, phase distortion, power amplifier, satellite transponder.**

I. Introduction

Spectrum and power efficiencies are becoming the most important aspects of any base-station transmitter or satellite transponder design for satellite communications (satcom) applications [1]–[4]. In particular, to achieve spectrum efficiency, multilevel digital modulation techniques such as n/π QPSK and 16 quadrature amplitude modulation (QAM) or 256 QAM, as well as time-division multiple access (TDMA)/code-division multiple-access (CDMA) techniques have been introduced and used. These techniques give rise to fluctuating envelope signals that are sensitive to any nonlinearities in the communication system. The power amplifiers (PA's) either solid-state power amplifiers (SSPA's) or traveling-wave tube amplifiers (TWTA's) of the transmitter/transponder are the most contributors in generating these nonlinearities. Therefore, the performances of theses PA's in terms of power consumption and linearity directly affect the transmission capacity of the satellite system. In principle, it is relatively easy to measure the power efficiency of a PA, however it is often, more difficult to measure the complex nonlinear distortion of a PA. Such characterization calls, in principle, for a use of amplitude and phase measurement systems like automated network analyzers. These kinds of instruments are not commonly available and require sophisticated calibration procedures. In addition, for flight (off-ground) testing, these phase measurements become quasi-nonfeasible to perform. In this paper, we propose a new method to carry out AM–AM and AM–PM distortion characterization of microwave communication circuits, subsystems, or systems using only power-detection techniques. The proposed method uses an unequal three-tone signal (UTTS) to drive the nonlinear device-under-test (NDUT). This NDUT could be a PA or even a frequency-translating device such as a satellite transponder. The measurements of the tone levels of an UTTS at the input and output of the NDUT allows the calculation of AM–AM compression factor and the AM–PM conversion coefficient of the NDUT for any operating carrier frequency and power level. The formulation of the problem and the close-form analytical solution is presented. To validate, the technique computer simulations were carried out using HP-EEsof Series IV software suites. Simulation results obtained on a 60-dB gain 100-W TWT amplifier are presented. Its measured AM–AM and AM–PM distortion curves modeled the nonlinear behavior of this TWTA.

Manuscript received May 1, 1998. The work of F. M. Ghannouchi was supported by the Japan Science and Technology Corporation under the Science and Technology Agency Program.

F. M. Ghannouchi is with the Kashima Space Research Center, Kashima-shi, Ibaraki 314-0012, Japan, on leave from the Ecole Polytechnique, Montreal, P.Q., Canada H3C 3A7

H. Wakana and M. Tanaka are with the Communication Research Laboratory, Kashima Space Research Center, Kashima-shi, Ibaraki 314-0012 Japan.

Publisher Item Identifier S 0018-9480(00)06540-6.

II. Formulation of the Problem

A memoryless nonlinear high PA excited by microwave signal having a certain frequency bandwidth $2\Delta w$ centered around a carrier frequency w such that $\Delta w << w$ can be characterized by its envelope AM–AM and AM–PM distortion curves [5]. The RF input to the PA can be expressed by

$$v_{\rm in}(t) = A(t)\,\cos\Big[wt + \theta(t)\Big]. \tag{1}$$

The corresponding output signal $v_{\rm out}(t)$ can also be expressed by

$$v_{\rm out}(t) = G\Big[A(t)\Big]\,\cos\Big\{wt + \theta(t) + \Psi\Big[A(t)\Big]\Big\} \tag{2}$$

where $G[A(t)]$ and $\Psi[A(t)]$ are, respectively, the AM–AM and AM–PM distortion curves of the PA. We assume in this formulation that the PA has a flat complex gain over the $2\Delta w$ frequency bandwidth centered on the carrier frequency w, and the harmonic frequencies generated by the PA are filtered out before reaching the output of the PA.

In the case where the input signal is a superposition of a low-index sinusoidal AM signal and a low-phase deviation sinusoidal PM signal, (1) can be written as

$$v_{\rm in}(t) = A_0\Big[1 + \alpha\,\cos(\Delta wt)\Big]\,\cos\Big[wt + \beta\,\sin(\Delta wt) + \theta_o\Big] \tag{3}$$

where α and β are, respectively, the amplitude index of the AM signal and phase deviation of PM signal and, A_0 and θ_0 are the average amplitude and phase values of the AM and PM signals.

For small variations of the amplifier phase shift with the power level, it was demonstrated that the PA phase-shift variation is proportional to the input power level alternatively proportional to the square of the input signal envelope [5], therefore, one can write (2) as follows:

$$v_{\rm out}(t) = GA_0\Big[1 + \alpha\Big((1-c)\,\cos(\Delta wt)\Big)\Big] \cdot\cos\Big[wt + \theta_0 + \Delta\theta + \beta\,\sin(\Delta wt) + k_p\alpha\,\cos(\Delta wt)\Big] \tag{4}$$

where G is the operating voltage gain of the PA

$$c = 1 - \frac{(\Delta v_{\rm out}/v_{\rm out})}{(\Delta v_{\rm in}/v_{\rm in})} \tag{5a}$$

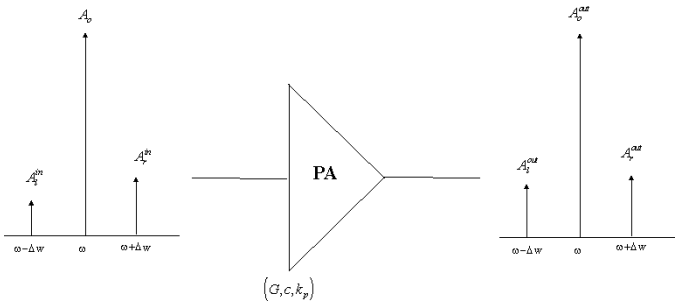

Fig. 1. Block diagram illustrating the UTTS method.

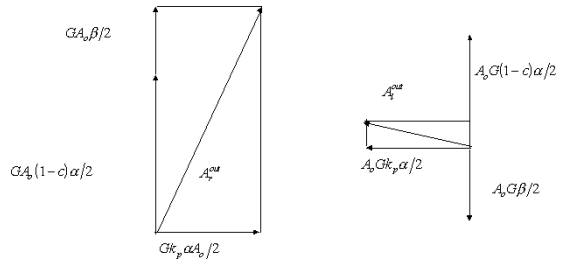

Fig. 2. Diagram illustrating the vector addition of the sidebands of the UTTS method.

is the AM–AM compression factor of the PA and

$$k_p = \frac{\Delta\theta}{\alpha} \tag{5b}$$

is the AM–PM conversion coefficient of the PA and $\Delta\theta$ is the peak phase change due to AM–PM conversion.

It is worth noticing that when the amplifier is in far backoff, operating in its linear region, $c = 0$, and when the amplifier is completely saturated, operating as perfect limiter, $c = 1$.

In recapitulation, G, c, and k_p are the parameters that characterize the PA and A_o, α, and β are the parameters that characterize the input signal.

In the frequency domain, the input signal can be seen as the superposition of unequal three sinusoidal tones: the carrier and two unequal sides band tones generated by AM and PM.

Fig. 1 shows a schematic diagram of the input signal spectrum, PA, and output signal spectrum. It is important to notice that the relative levels of the two output sidebands are different from the level of the two input sidebands. This is basically due to the nonlinear behavior of the PA, which introduces an extra AM due to AM–AM distortion and an extra PM due to AM–PM conversion.

One can summarize by saying that we are attempting to solve the problem that consists of calculating G, c, and k_p as functions of the amplitudes of an UTTS at the input as well at the output of the PA.

III. Analytical Solution

For a low-index AM signal, it is well known that the two sidebands are in phase. However, for a low-phase deviation PM carrier, the closest two sidebands to the carrier are out of phase. Therefore, one can write, in the frequency domain, the following expression for a given low-index AM signal:

$$v_{\rm in}^{AM}(t) = (A_0/2)\cos(wt) + (\alpha A_0/2)\cos\Big[(w+\Delta w)t\Big] + (\alpha A_0/2)\cos\Big[(w-\Delta w)t\Big] \tag{6}$$

and the following expression for a given low-phase deviation PM signal:

$$v_{\rm in}^{\rm PM}(t) \cong (A_0/2)\cos(wt) + (A_0\beta/2)\cos\Big[(w+\Delta w)t\Big] - (A_0\beta/2)\cos\Big[(w-\Delta w)t\Big] \tag{7}$$

where $A_0/2$ is the amplitude of the carrier for both AM and PM signals and α and β are, respectively, the index of the AM signal and the phase deviation of the PM signal.

In (7), we assume that $\beta \approx 0$; which is practically equivalent to proclaim that the energy contained in higher order sidebands is negligible in comparison with first-order sidebands of the PM signal.

The superposition of the two AM and PM signals gives

$$\begin{aligned} v_{\rm in}(t) &\cong v_{\rm in}^{\rm AM}(t) + v_{\rm in}^{\rm PM}(t) \\ &= A_0\cos(wt) + A_r^{\rm in}\cos\Big[(w+\Delta w)t\Big] + A_l^{\rm in}\cos\Big[(w-\Delta w)t\Big] \\ &= A_0\cos(wt) + \Big[A_0(\alpha+\beta)/2\Big]\cos\Big[(w+\Delta w)t\Big] + \Big[A_0(\alpha-\beta)/2\Big]\cos\Big[(w-\Delta w)t\Big]. \end{aligned} \tag{8}$$

From (8), one can deduce that α and β can be obtained just by measuring the levels of the right- and left-hand sidebands around the carrier as follows:

$$\alpha = \frac{A_r^{\rm in} + A_l^{\rm in}}{A_0} \quad \text{and} \quad \beta = \frac{A_r^{\rm in} - A_l^{\rm in}}{A_0}. \tag{9}$$

We assume in the above equations that $\beta \le \alpha$

As has been mentioned before, the AM sidebands of the input signal will be compressed by the PA due to AM–AM compression, and an additional PM sidebands will be generated by the PA due to its AM–PM conversion. These newly generated PM sidebands are 90° out of phase relative to the others two sidebands [6]. The vector addition of these sidebands, as shown in Fig. 2, leads to

$$\left(A_r^{\rm out}\right)^2 = G^2\left[\frac{(1-c)A_0\alpha + A_0\beta}{2}\right]^2 + \left(\frac{Gk_pA_0\alpha}{2}\right)^2 \tag{10a}$$

$$\left(A_l^{\rm out}\right)^2 = G^2\left[\frac{(1-c)A_0\alpha - A_0\beta}{2}\right]^2 + \left(\frac{Gk_pA_0\alpha}{2}\right)^2 \tag{10b}$$

where $A_r^{\rm out}$ and $A_l^{\rm out}$ are, respectively, the magnitudes of right- and left-hand sidebands at the output of the PA.

Substituting (9) into (10a) and (10b), one can write

$$R_1^2 = (c-x_1)^2 + k_p^2 \tag{11a}$$

$$R_2^2 = (c-x_2)^2 + k_p^2 \tag{11b}$$

where $x_1 = 2A_r^{\rm in}/(A_r^{\rm in} + A_l^{\rm in})$, $x_2 = 2A_l^{\rm in}/(A_r^{\rm in} + A_l^{\rm in})$, $R_1 = (2A_r^{\rm out}/G(A_r^{\rm in} + A_l^{\rm in}))$, $R_2 = (2A_l^{\rm out}/G(A_r^{\rm in} + A_l^{\rm in}))$, and $G = A_0^{\rm out}/A_0$.

It is to be noticed that (11a) and (11b) are two circle equations in the $(c,\ k_p)$ plane. The centers and radii of these two circles are x_1 and x_2 and R_1 and R_2, respectively. The common intersection of these two circles, as shown in Fig. 3, gives c and k_p values of the PA for a given operating frequency w and a given input carrier pour level A_0.

The analytical solution of the set of equations (11a) and (11b) leads to the following close-form expressions for c and k_p:

$$c = \frac{R_2^2 - R_1^2 + (x_2+x_1)(x_1-x_2)}{2(x_1-x_2)} \tag{12a}$$

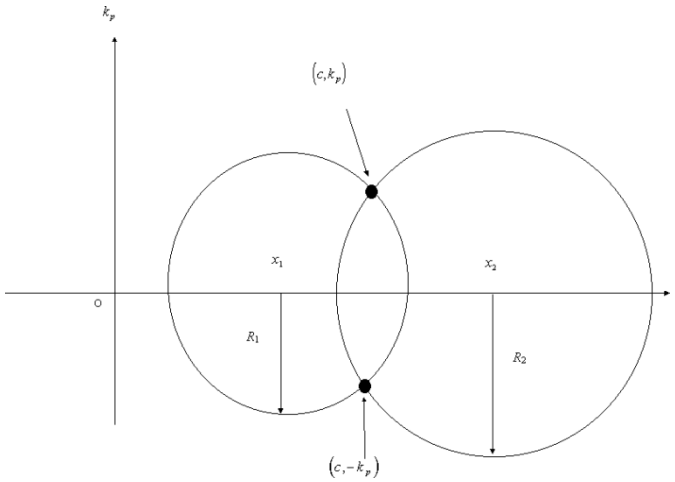

Fig. 3. Graphical solution of the UTTS method.

and

$$k_p = \pm\sqrt{R_1^2 - (c - x_1)^2}. \tag{12b}$$

IV. Discussion

We felt it valuable and of worth to readers of this paper to make the following comments about the UTTS method and to draw some conclusions about its validity and suitability for the characterization of PA's in satcom applications.

1) It is to be noted in (12b) that the positive as well as negative values of k_p are both solutions in the mathematical sense, therefore, one has to know in advance the sign of k_p.
2) The UTTS technique can be used for the characterization of amplification systems as well as for frequency-translating devices and systems such as a single-sideband (SSB) up converter, SSB down converter, or even for a satellite transponder. The only change in the testing conditions is that the AM and PM signals at the input and output have two different carrier frequencies.
3) The technique described in [6] and designated as the UB2T method in [2], which uses unbalanced two tones, is accounted for in the UTTS method. The selection of testing conditions in such a way that $\alpha = \beta$, which is equivalent to $A_l^{\text{in}} = 0$, implies that the center of the second circle x_2 is placed at the origin of the $(c,\ k_p)$ plane, consequently, the UB2T method can be considered as a particular case of UTTS method. In addition, it is also expected that for a low-level input drive signal, the accuracy of the UTTS method is better than the accuracy of the UB2T method. Since, for a low-input signal level, the radius R_2 is very small in comparison to R_1, a non-well-defined intersection of the two circles will turn up, which leads to nonaccurate c and k_p solutions for the UB2T method.
4) Either the UB2T or UTTS assume that modulation frequency bandwidth must be much smaller than (1), the time constant of the PA biasing circuit, and (2), the time constant of any extra gain or level control circuit that might be included in the PA to be tested.
5) The UTTS method cannot be used if the carrier is only AM ($\beta = 0$) or only PM ($\alpha = 0$). Either condition leads to a reduction of the set of equations (10a) and (10b) to one equation with two unknowns, which has an infinite number of solutions and cannot yield to unambiguous solutions for c and k_p.
6) The determination at each input power level of the AM–PM (AM–AM) conversion coefficient (compression factor) by the differentiation of the one-tone AM–PM $\phi = f(P_{\text{in}})$ (AM–AM, $P_{\text{out}} = g(P_{\text{in}})$) static measurement curve leads to reasonably accurate results only if the PA is quasi-memoryless and does not includes extra biasing or control circuits that have nonnegligible time constants. Besides that, the static measurement characterization technique tends to underestimate the nonlinear behavior of the PA in comparison to dynamic measurement characterization techniques such as the UTTS method.
7) The UTTS technique cannot be used to determine the linear distortion (complex gain variation with frequency) of the PA as a function of the frequency by just sweeping the carrier frequency while keeping the sidebands at Δw away from the carrier and maintaining the UTTS signal at the same power levels. It obvious from the analytical formulation any change in the operating gain will affect both the carrier and sidebands in the same manner, therefore, their relative amplitudes remain the same and the c and k_p calculated values will not change.
8) The UB2T signal used in [2] to measure the linear distortion (variation of the gain with frequency) of the TWTA of COMETS satellite's transponder, which includes a driver and an automatic level control (ALC) circuit to maintain a constant saturated output power, deserves, in our opinion, further justifications and explanations about its suitability to insure a reasonable level of accuracy and confidence in the results obtained over a 120-MHz bandwidth. One can argue that the sweeping of the frequency of the sideband away from the fixed frequency carrier while (1) keeping a high enough carrier power driving the amplifier that secures that the TWTA is operated in the compression region and even in the saturation region (2) and maintaining, during the frequency sweep, the same power levels of the two tones at the input of the PA, can be used to deduce the linear distortion of the PA from the measurements of the sideband level variation with frequency. This is correct and sound only if the PA is quasi-memoryless and has no feedback loops and has biasing circuits with a near-zero time constant. In our opinion, these conditions are far way to be satisfied for the 100-dB gain and 200-W amplification system, as described in [1].
9) Based on what we have mentioned in 4) and 8), it is expected that, by carrying out the TWTA linear distortion characterization using an UTTS/UB2T signal while sweeping the sidebands over a narrow modulation frequency bandwidth, the accuracy and confidence on the results that would be obtained will be much better. In our opinion, the measurement of the linear distortion over the 120-MHz bandwidth could be performed accurately if the 120-MHz modulation bandwidth is divided, let us say, in 120 1-MHz sub-modulation bands, where sidebands of UTTS/UB2T signal can be swept successively 120 times, over only 1-MHz sub-modulation band each time. Therefore, the carrier and sidebands have to be displaced, 120 times to cover the original 120-MHz modulation bandwidth before sweeping the sidebands over the 1-MHz sub-modulation bandwidths.

V. Simulation Results

In order to validate the technique, the measured AM–AM and AM–PM curves of a 60-dB gain and 100-W TWT amplifier, shown in Fig. 4, were used to model the nonlinear behavior of this amplifier [1]. From these curves, gain compression and phase-variation data relative to small-signal gain and phase values were extracted and entered in the HP-EEsof Series IV software to model the nonlinear behavior of the TWTA. A three-sinusoidal-source test bench was used

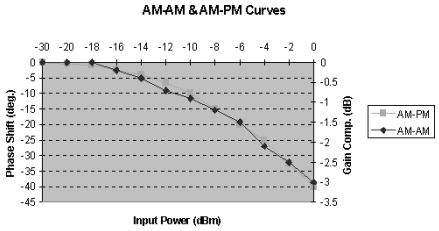

Fig. 4. AM–AM and AM–PM curves of a TWTA.

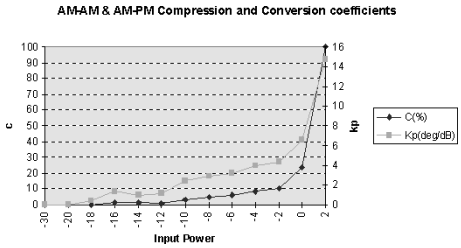

Fig. 5. AM–AM and AM–PM compression and conversion coefficients of a TWTA.

to generate the UTTS signal. The input power of the carrier was varied from -30 to 0 dBm while keeping a difference of 30 dB between the carrier level and the level of highest (right-hand side) sideband signal. The difference between the right- and left-hand sideband signals was maintained to 3 dB during carrier power sweep. The carrier frequency was 20 GHz and the sidebands were 1 MHz away from the carrier. Fig. 5 shows the AM–AM compression factor and the AM–PM conversion factor variations when the input power of the amplifier is swept. These results are in good agreement with those that can be deduced from static one-tone measurements by the differentiation of the $P_{\rm out} = g(P_{\rm in})$ curve and $\phi = f(P_{\rm in})$, except for the last point ($P_{\rm in} = 2$ dB) where AM–AM and AM–PM distortion data were not defined (see Fig. 4).

VI. Conclusion

In this paper, we proposed a new method to measure AM–AM and AM–PM compression and phase conversion factors of any amplification systems or frequency-translating devices or systems using only power measurements. The proposed technique is based on the use of an UTTS to stimulate any nonlinear devices or systems It was demonstrated that the tone levels of an UTTS at the input and output of the NDUT are related to the AM–AM compression factor and AM–PM conversion coefficient of the NDUT by two quadratic equations. The solution of this nonlinear system gives the values of the AM–AM compression factor and AM–PM conversion coefficient for any carrier frequency and power level. Validation of this technique was carried out using the HP-EEsof Series IV software suite. Simulation results obtained for a 60-dB gain and 100-W TWTA prove the validity and the effectiveness of the UTTS technique. We are planing to use the UTTS method for off-ground testing of the TWTA's transponder of the COMETS satellite this autumn.

Acknowledgment

The authors would like to thank M. Ohkawa, Communications Research Laboratory, Kashima Space Research Center, Kashima, Japan, for his time and the helpful discussions about the UB2T method. Author F. M. Ghannouchi would also like to acknowledge the Communications Research Laboratory (CRL), Kashima Space Research Center, Kashima-shi, Ibaraki, Japan, for access to pertinent software and hardware facilities to accomplish this paper in collaboration with his co-authors.

References

[1] M. Kurahashi, H. Kubo, and S. Hamada, "Ka-band 80-100 W TWT for satellite," in *17th AIAA Int. Commun. Satellite Syst. Conf.*, Yokohama, Japan, Feb. 23–27, 1998, paper AIAA-98-1278.

[2] M. Iguchi, M. Ohkawa, T. Takahashi, H. B. Li, and H. Oohashi, "High-speed trellis-coded 8-PSK modulation in the 21-GHz band performance in the final on-ground test of the COMETS satellite," in *3rd Ka-Band Utilization Conf.*, Sorrento, Italy, Sept. 15–18, 1997, pp. 91–96.

[3] A. M. Khilla and D. Leuch, "Linearized *L/C*-band SSPA/up converter for mobile communication satellite," in *16th AIAA Int. Commun. Satellite Syst. Conf.*, Washington, DC, Feb. 1997, paper AIAA-96-09 880.

[4] F. M. Ghannouchi, G. Zhao, and F. Beauregard, "Simultaneous AM–AM/AM–PM distortion measurements of microwave transistors using active load-pull and six-port techniques," *IEEE Trans. Microwave Theory Tech.*, vol. 43, pp. 1584–1588, July 1995.

[5] R. G. Medhurst, J. H. Roberts, and W. R. Walsh, "Distortion of SSB transmission due to AM–PM conversion," *IEE Trans. Commun. Syst.*, pp. 166–176, June 1964.

[6] L. P. Laico, H. L. McDowell, and C. R. Moster, "A medium power traveling-wave tube for 6000-Mc radio relay," *Bell Syst. Tech. J.*, pp. 1285–1346, Nov. 1956.

A 500-mW High-Efficiency Si MOS MMIC Amplifier for 900-MHz-Band Use

Noriaki Matsuno, Hitoshi Yano, Yasuyuki Suzuki, Toshiro Watanabe, Shigeki Tsubaki, Tetsu Toda, and Kazuhiko Honjo

***Abstract*—A 500-mW monolithic-microwave integrated-circuit (MMIC) amplifier using a 0.6-μm Si MOSFET for 900-MHz-band use has been developed. The input matching network, which consists of a spiral inductor and an MOS capacitor, was integrated onto the chip using a low-cost mass-production large-scale-integration process. A new spiral-inductor model, taking into account the dielectric loss and skin effect of the Si substrate, was introduced. We analyzed the stability and gain dependence on the gate structure of the MOSFET and optimized the gate finger length and the loss of the matching network to achieve high gain and stability. The fabricated MMIC amplifier achieved a linear gain of 15.2 dB and an output power of 27.1 dBm with a PAE of 60% under a supply voltage of 4.8 V.**

***Index Terms*—Cellular phone, GSM, MMIC, power amplifier, Si MOSFET, spiral inductor.**

I. Introduction

Low-cost power amplifiers for cellular phones are strongly required since the power amplifier is one of the most expensive components. Silicon power MOSFET's [1]–[5] are inherently superior in terms of

Manuscript received April 23, 1999.

N. Matsuno, H. Yano, and Y. Suzuki are with Photonic and Wireless Devices Research Laboratories, System Devices and Fundamental Research, NEC Corporation, Ibaraki 305-8501, Japan.

T. Watanabe is with Compound Semiconductor Device Division, NEC Corporation, Kanagawa 211-8666, Japan.

S. Tsubaki and T. Toda are with Semiconductor Division, NEC Kansai, Shiga 520-0833, Japan.

K. Honjo is with System Devices and Fundamental Research, NEC Corporation, Ibaraki 305-8501, Japan.

Publisher Item Identifier S 0018-9480(00)06538-8.

cost. For further cost reduction, monolithic-microwave integrated-circuit (MMIC) amplifiers based on Si MOSFET technology will be one of the strong candidates.

The drawback of the Si MMIC technology is the large loss of the passive elements on the conductive Si substrate. Thus, previously reported Si MOS MMIC power amplifiers required some improved fabrication technologies, e.g., a thick metal or dielectric layer process for inductors or a special dielectric layer process for capacitors [7], [8].

In this paper, we describe an Si MOS MMIC amplifier for 900-MHz-band use, fabricated using a low-cost mass-production large-scale-integration (LSI) process with two-level wiring. To overcome the drawback of the Si MMIC technology, we analyzed the stability and gain dependence on the gate structure of the MOSFET, and optimized the gate structure and loss of the matching network. Thus, the large loss of the on-chip matching network stabilizes the MMIC operation, and high gain was achieved.

II. Design and Fabrication

A block diagram of a two-stage Si MOSFET power amplifier for 900-MHz-band global system for mobile communications (GSM) use is shown in Fig. 1(a). We integrated the first-stage MOSFET and the input 50-Ω matching network onto the Si substrate. Our discrete MOSFET's for use in the final stage have achieved an output power of 35 dBm with a power gain of 10 dB. Thus, the output power of the MMIC must be above 25 dBm.

The circuit diagram of the MMIC is shown in Fig. 1(b). The input matching network consists of a spiral inductor and an MOS capacitor. The diodes to protect the MOSFET from static damage were also integrated. The MMIC was designed using the harmonic-balance simulator Series IV. The MOSFET's were simulated with a MOSFET LEVEL3 model [4], [9]. The chip photograph is shown in Fig. 1(c). The chip size was 1.2 × 1.25 mm.

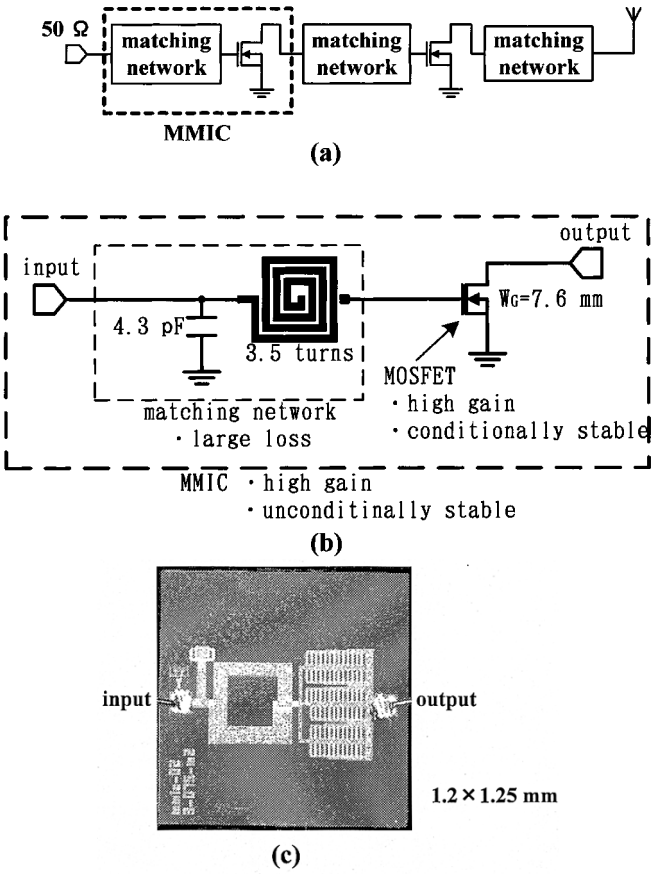

Fig. 1. (a) Block diagram of a two-stage Si MOSFET power amplifier for 900-MHz-band GSM use. (b) Circuit diagram of the MMIC. (c) Chip photograph of the MMIC.

A. MOSFET Design

We used a 0.6-μm WSi gate power MOSFET [4], [5]. Each n^+ source was connected to the adjacent p^+ region by Al wiring. Thus, the source is directly connected to the ground through the p^+ Si substrate, which reduces the parasitic inductance and maximizes RF gain [5].

The gatewidth of power MOSFET's is much larger than that of GaAs FET's since the drain current density of the MOSFET's is lower. An increase in the gatewidth decreases the input and output impedance of the device, resulting in a large matching loss [4]. Thus, the gatewidth should be minimized to ensure sufficient output power. Fig. 2 shows the gatewidth dependence of the simulated output power at the 3-dB-gain compression point under a supply voltage of 4.8 V. This figure shows that a gatewidth of over 4.7 mm is required to achieve an output power above 25 dBm. We selected a gatewidth of 7.6 mm to ensure an output power margin of 2 dB.

The gate finger design is important to achieve high gain. Fig. 3 shows the simulated maximum stable gain (MSG) and maximum available gain (MAG) as a function of the gatewidth per finger, also known as the gate finger length. When the finger length is more than 165 μm, a frequency of 900 MHz is in the MAG region, i.e., the MOSFET is unconditionally stable at 900 MHz. In this case, however, a low-loss matching network is required to maintain high gain. When the finger length is less than 165 μm, a frequency of 900 MHz is in the MSG region, i.e., the MOSFET is conditionally stable at 900 MHz. In that case, the loss of the matching network can stabilize the MMIC operation, and causes less gain reduction compared to the case when the MOSFET is unconditionally stable. We designed the finger length and the on-chip matching network to achieve both high gain and low return loss, and decided on a gate finger length of 50 μm. Accordingly, a high gain was achieved by using a low-cost mass-production LSI process.

B. Passive Element Design

The spiral inductor was fabricated using conventional two-level Al interconnections. The cross-sectional view of the inductor is shown in Fig. 4(a). The metal thickness was 0.5 μm for the first layer and 1.6 μm for the second layer. The spiral was fabricated using these layers connected in parallel by via to reduce the series parasitic resistance, except in the underpass region.

The inductor model should take into account the dielectric loss due to the Si substrate. In addition, we used an Si substrate with resistivity of 14 mΩ · cm, thus, the skin-effect mode appears [10]. The conventional π-type lumped-element model cannot take into account it. We introduced a new semilumped-element model [shown in Fig. 4(b)]. The inductor L_1 represents an spiral inductor model on dielectric substrates, which is implemented with most of microwave circuit simulators. Here, the microwave simulator Series IV allow us to use a function of the frequency for the substrate thickness parameter, thus, the skin-effect mode can be modeled. The lumped capacitors and resistors represent the parasitic elements due to the Si substrate. The model parameters were extracted from the measured S-parameters.

We decided upon the outer dimensions of 400 × 400 μm, the linewidth and spacing of 20 μm and 2 μm, and the number of turns of 3.5; these were selected to optimize the tradeoff between the loss and chip size. Here, the line spacing was narrow compared to the linewidth. However, the parasitic capacitance between adjacent lines

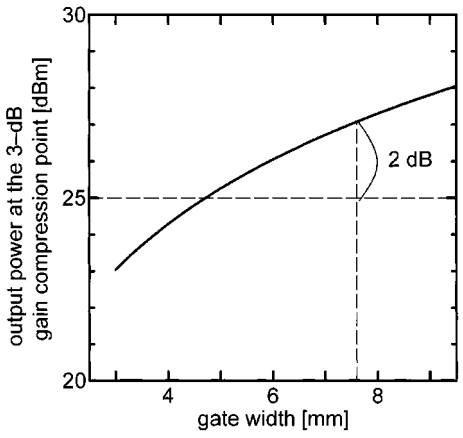

Fig. 2. Simulated output power as a function of the gatewidth of the MOSFET. The supply voltage was 4.8 V and the frequency was 900 MHz.

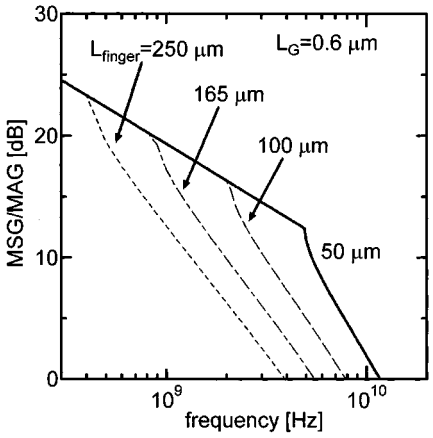

Fig. 3. Simulated MSG and MAG dependence on the gate finger length (L_{finger}).

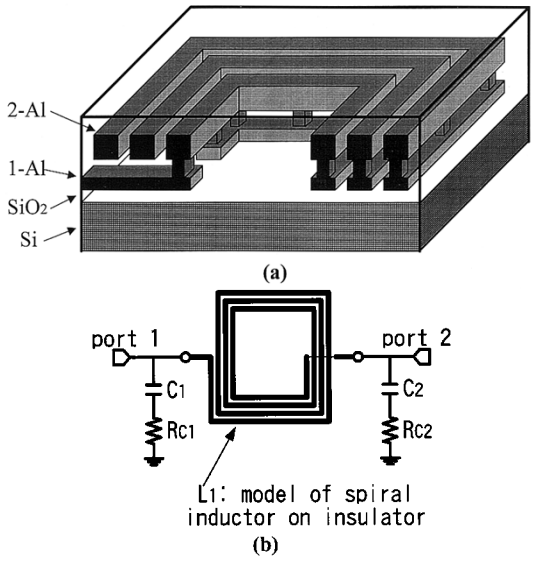

Fig. 4. (a) Cross-sectional view of the inductor. (b) Semilumped-element model for the spiral inductors on the Si substrate.

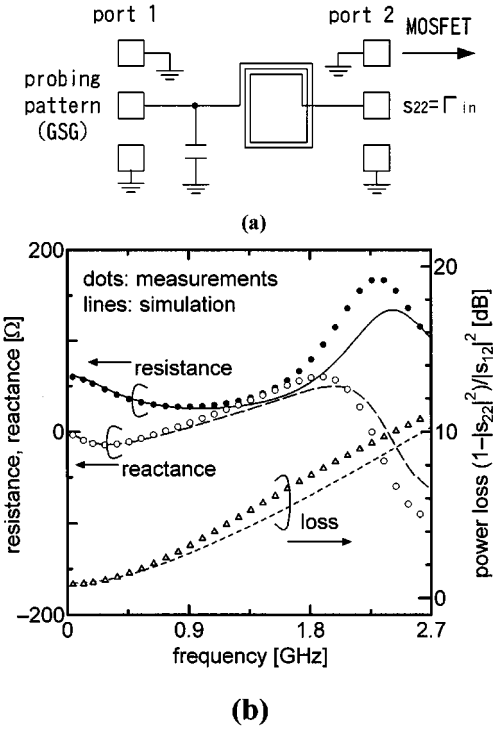

Fig. 5. (a) Schematic view of the test pattern for S-parameter measurement of the input matching network. (b) Resistance and reactance calculated from s_{22}, which correspond to the signal-source impedance for the MOSFET and the insertion power loss $|s_{12}|^2/(1-|s_{22}|^2)$.

is negligible since parasitic capacitance due to the Si substrate is much larger.

The MOS capacitor was fabricated by using the gate process. The gate oxide film was used as the capacitor dielectric. The measured quality factor of the MOS capacitor was more than 30 at 900 MHz.

III. RF Performance

The fabricated on-chip matching network was evaluated by using a test pattern shown in Fig. 5(a), which consisted of the matching network and ground–signal–ground probing patterns. In the MMIC, port 1 will be connected to the 50-Ω input line, and port 2 will be connected to the gate. Thus, s_{22} corresponds to the signal-source reflection coefficient for the MOSFET. Fig. 5(b) shows the resistance and reactance calculated from s_{22} and the insertion power loss. The simulated results agreed well with the measurements up to the third-harmonic frequency. Fig. 6(a) shows the power characteristics of the fabricated MMIC under a supply voltage of 4.8 V at a frequency of 900 MHz. The difference between the simulated results and the measurements were less than 1-dB gain and 3% in PAE. Fig. 6(b) shows the measured S-parameters using an off-chip output matching network. The $|s_{11}|$ and $|s_{22}|$ at 900 MHz were -19 dB and -6.3 dB, respectively. These results confirm the accuracy of our design technique.

The fabricated MMIC shows a linear gain of 15.2 dB and an output power of 27.1 dBm with a PAE of 60% at an input power of 16 dBm, as shown in Fig. 6(a). Although this MMIC was fabricated by using a low-cost mass-production LSI process with two-level Al interconnections, the gain and PAE were comparable to those for discrete MOSFET's. The amplifier maintained excellent performance even under a lower supply voltage of 3.4 V. In this case, a linear gain

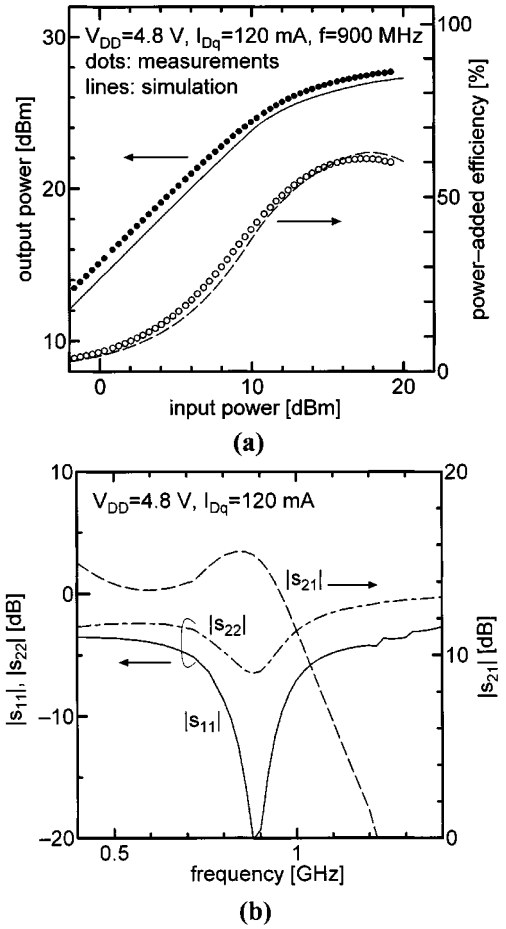

Fig. 6. (a) Power characteristics of the Si MOS MMIC amplifier under a supply voltage of 4.8 V. (b) S-parameters of the MMIC under a supply voltage of 4.8 V.

of 14.3 dB and an output power of 24.1 dBm with a PAE of 57% and a power gain of 10.1 dB were achieved.

IV. Conclusion

We have described an Si MOS MMIC amplifier for 900-MHz-band use fabricated by using a low-cost mass-production LSI process. We analyzed the stability and gain dependence on the gate structure of the MOSFET, and optimized the loss of the matching network and gate structure to achieve high gain and stability. The fabricated MMIC achieved a linear gain of 15.2 dB and an output power of 27.1 dBm with a PAE of 60% under a supply voltage of 4.8 V.

Acknowledgment

The authors would like to thank T. Inoue, Compound Semiconductor Device Division, NEC Corporation, Kanagawa, Japan, and T. Hirayama, Photonic and Wireless Devices Research Laboratories, System Devices and Fundamental Research, NEC Corporation, Ibaraki, Japan, for their invaluable contributions to the mask design, device fabrication, and the RF measurements. The authors are also grateful to T. Noguchi, Compound Semiconductor Device Division, NEC Corporation, Kanagawa, Japan, for his valuable advice, support, and encouragement throughout this paper's work.

References

[1] G. Ma *et al.*, "High efficiency submicron gate LDOMS power FET for low voltage wireless communications," in *IEEE MTT-S Int. Microwave Symp. Dig.*, 1997, pp. 1303–1306.
[2] I. Yoshida *et al.*, "A highly efficient 1.9-GHz Si high-power MOS amplifier," *IEEE Trans. Electron Devices*, vol. 45, pp. 953–956, Apr. 1998.
[3] ——, "A 3.6-V, 4-W, 0.2-cc Si power–MOS–amplifier module for GSM handset phones," in *ISSCC'98 Tech. Dig.*, pp. 50–55.
[4] N. Matsuno *et al.*, "Large-signal analysis of power MOSFET's and its application to device design," *IEICE Trans. Electron.*, vol. E80-C, pp. 734–739, 1997.
[5] T. Watanabe *et al.*, "'A 3 V operation power MOSFETs for DCS1800 and GSM RF amplifier," in *Asia–Pacific Microwave Conf. Dig.*, 1998, pp. 1175–1177.
[6] D. Ngo *et al.*, "RF silicon MOS integrated power amplifier for analog cellular applications," in *IEEE MTT-S Int. Microwave Symp. Dig.*, 1996, pp. 559–562.
[7] C. Dragon *et al.*, "A silicon MOS process for integrated RF power amplifiers," in *IEEE MTT-S Int. Microwave Symp. Dig.*, 1996, pp. 257–260.
[8] J. N. Burghartz *et al.*, "Microwave inductors and capacitors in standard multilevel interconnect silicon technology," *IEEE Trans. Microwave Theory Tech.*, vol. 44, pp. 100–104, Jan. 1996.
[9] A. Vladimirescu and S. Liu, "The simulation of MOS integrated circuits using SPICE2," Electron. Res. Lab., Univ. California Berkeley, Berkeley, CA, Memo. UCB/ERL M80/7, 1980.
[10] H. Hasegawa *et al.*, "Properties of microstrip line on Si–SiO_2 system," *IEEE Trans. Microwave Theory Tech.*, vol. MTT-19, pp. 869–881, Nov. 1971.

Direct Measurement of Crosstalk Between Integrated Differential Circuits

David E. Bockelman and William R. Eisenstadt

***Abstract*—Silicon integrated-circuit test structures have been fabricated that allow direct measurement of crosstalk between differential transmission lines and between single-ended transmission lines in the presence or absence of a metal ground plane. The differential test structures are characterized with mixed-mode scattering parameters (common mode, differential mode, and mode conversion), as measured with the pure-mode vector network analyzer. Comparisons with simulation show good agreement for differential-mode crosstalk, and the dependence of crosstalk on transmission-line separation is presented. Difficulties in simulating crosstalk for even simple structures illustrate the utility of direct measurement of crosstalk.**

***Index Terms*—Crosstalk, differential circuits, network measurements, scattering parameters.**

I. Introduction

In many integrated-circuit (IC) applications, unintended coupling (or crosstalk) of signals between circuits can be a critical performance limitation. Differential circuit topology is being adopted in IC's due to its increased crosstalk immunity and increased dynamic range over ground referenced (single-ended) circuits. Differential circuits

Manuscript received May 4, 1999.

D. E. Bockelman is with the Motorola Florida Communications Research Laboratory, Plantation, FL 33322 USA (e-mail: d.bockelman@ieee.org).
W. R. Eisenstadt is with the Department of Electrical and Computer Engineering, University of Florida, Gainesville, FL 32611 USA.

Publisher Item Identifier S 0018-9480(00)06537-6.

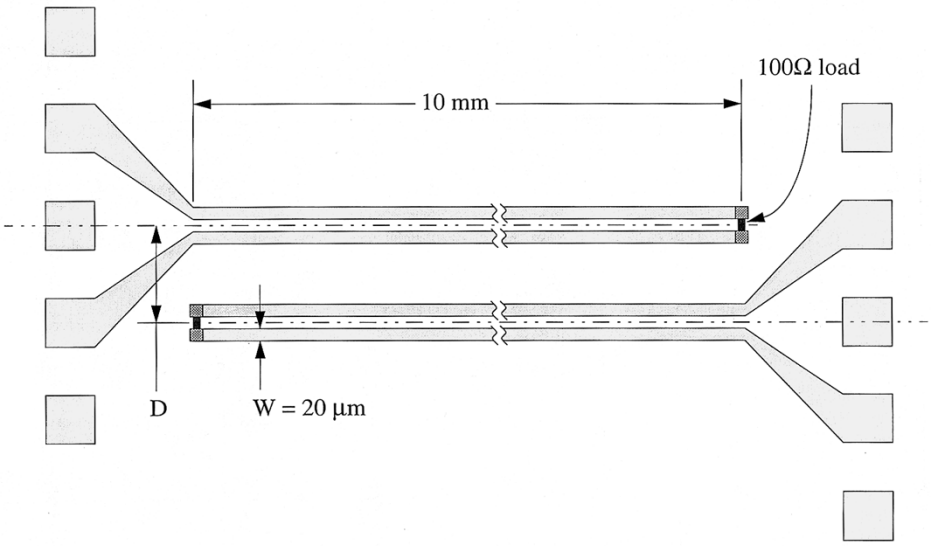

Fig. 1. Top view of structure for measuring crosstalk between differential transmission lines.

crosstalk must be either verified to be acceptably low or reduced to an acceptable level in sensitive applications.

Circuit-to-circuit crosstalk is highly dependent on the circuits and structures involved. Circuit topologies, impedance levels, physical layout, and IC technology all play critical roles in determining crosstalk strength. Crosstalk between two complex circuits can be difficult to measure, simulate, or predict due to the large dynamic-range requirements for such a measurement and the lack of accurate RF differential measurement capability.

This paper describes a method for the direct measurement of crosstalk between simple differential and single-ended integrated transmission lines. The direct measurement of differential circuits is accomplished with a recently developed pure-mode vector network analyzer (PMVNA) [1]. The PMVNA measures the differential- and common-mode responses of a device in terms of mixed-mode scattering parameters (s-parameters) [2]. The accurate measurement of these mixed-mode s-parameters and the increased dynamic range compared to single-ended measurement has been demonstrated on-wafer [3]–[5]. With these recent developments, the RF crosstalk between integrated differential circuits can be directly measured.

II. Crosstalk Experiment Definition

For this paper, crosstalk is examined for differential transmission lines and compared to single-ended transmission lines, where both lines are characterized with and without a metal ground plane. The basic crosstalk experiments consist of pairs of adjacent transmission lines, fabricated with aluminum on a silicon substrate, with each pair separated by a different distance, as shown in Fig. 1. The transmission lines used in the experiments are illustrated by the cross-section diagrams of Fig. 2; the experiments without a metal ground plane are the same, except the transmission lines are formed in the first metal. Each transmission line in the pair is terminated with a resistive load (100 Ω for differential lines, 50 Ω for single-ended lines), which allow two-port measurements of the transmission-line pairs, where the transmission (s_{dd21} for differential lines, s_{21} for single-ended lines) is the measured crosstalk.

Each transmission line is 10-mm long, not including the 100-μm-square probe pads. This relatively long length decreases the significance of end effects such as the probe pads and resistor loads. With such structures, the crosstalk of the transmission lines will dominate the measured crosstalk. Furthermore, the measured transmission will not be significantly affected by the probe-to-probe crosstalk. It has been shown, at separations and frequencies used in this paper, the probe-to-probe crosstalk and the crosstalk due to the probe pad structures will be less than −120 dB for the differential mode and less than −100 dB for the common mode (well below measured crosstalk) [6].

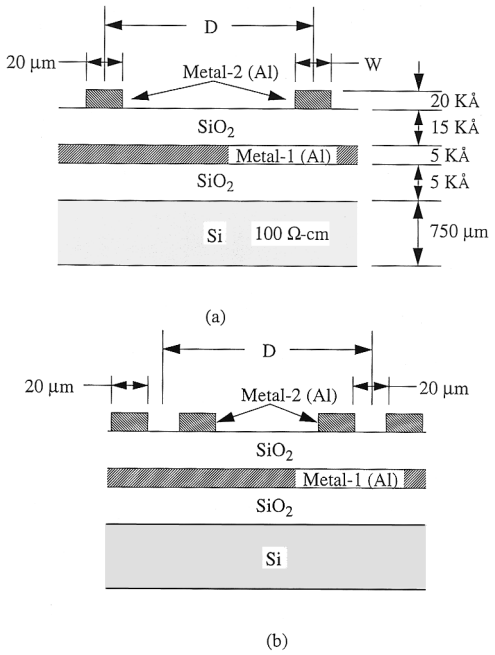

Fig. 2. Cross-sectional diagram representing some of the types of crosstalk experiments. (a) Two single-ended lines with metal ground plane. (b) Two differential line pairs with metal ground plane.

III. Measured Crosstalk of Transmission Lines Without Metal Ground Planes

This section describes the results of differential and single-ended transmission lines without a distinct metal ground plane. The measured line-to-line crosstalk of the differential and single-ended transmission

lines are summarized in Fig. 3. The solid lines in this figure show the various measured crosstalk at 1.0 GHz as a function of the normalized line separation. Crosstalk is measured as the magnitude of the transmission between the adjacent lines (i.e., S_{dd21}, S_{cc21}, etc.).

Also shown in Fig. 3 is the simulated line-to-line crosstalk of differential and single-ended transmission lines (dashed lines) as conducted in Hewlett-Packard's Microwave Design System (MDS) [7]. These structures are modeled as coupled microstrip transmission lines on a thick lossy dielectric of silicon ($\varepsilon_r = 11.9$, loss tangent $= 1.5$), as described in [8] and [9]. The dimensions of the microstrip model are that of the physical structure. The dielectric thickness is nominally 750 μm, but is forced to be less than 500 μm in most cases due the dimensional limits of the MDS coupled microstrip model. In the model, a ground plane is below the dielectric. The metal thickness of the signal lines is modeled at 0.5 μm with a conductivity of 2×10^6 Sie/m (approximately half that of bulk aluminum). Additionally, the differential structures have also been simulated with Hewlett-Packard's Momentum planar electromagnetic structure simulator [10] with very similar results.

As can be seen in Fig. 3, the agreement between measured and simulated crosstalk of the single-ended transmission lines is quite good, with reasonable agreement for the differential- and common-mode crosstalk between the differential transmission lines. The deviation between simulated and measured crosstalk is likely due to the maximum allowable substrate thickness in the model, which decreases as the line separation increases. The electromagnetic structure simulations (Momentum), which have no such limitations, agree more closely to measured data at these wide separations.

These measurement allow some basic observations about crosstalk between IC interconnections. Fig. 3 clearly shows the measurable reduction of crosstalk in the differential mode in comparison to the common mode and the single-ended line (20 dB at small separations and 70 dB at large separations). The measured differential crosstalk decreases nearly as the theoretical limit of $1/D^3$, where D is the line separation. The common-mode and single-ended crosstalk decrease approximately as $1/D$. The absolute level of crosstalk between transmission lines will roughly scale with transmission-line length (for $L < \lambda/4$), but the relative strength of the crosstalk for single-ended lines with respect to that of differential lines will be approximately independent of length. While this paper reports measured results at 1.0 GHz, these trends have been demonstrated across frequency [5], where the crosstalk strength is a function of line separation in terms of wavelength.

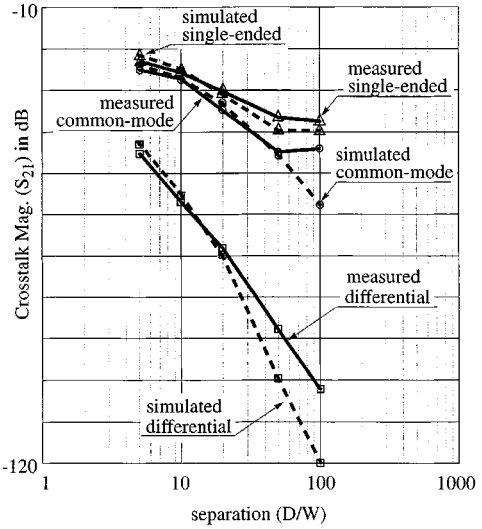

Fig. 3. Measured line-to-line crosstalk (at 1.0 GHz) for various transmission lines without metal ground planes as a function of line separation. Solid lines indicate measured data and dashed lines indicate simulated data.

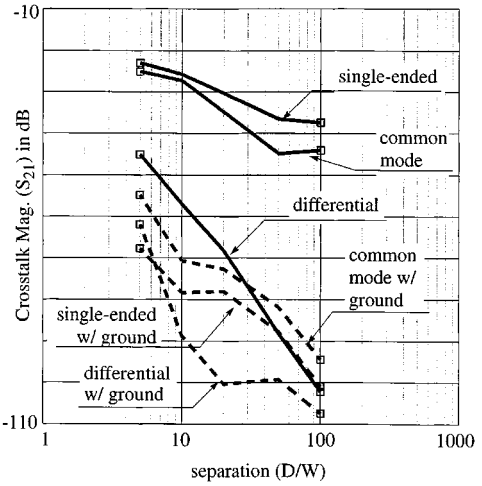

Fig. 4. Measured line-to-line crosstalk (at 1.0 GHz) for various transmission lines as a function of line separation. Solid lines indicate single-ended and differential transmission lines without metal ground planes. Dashed lines indicate single-ended and differential transmission lines with metal ground planes.

IV. Measured Crosstalk of Transmission Lines with Metal Ground Planes

This set of experiments examines the crosstalk performance of integrated transmission lines where a metal ground plane is used. These structures are the same as those in the previous section, except that first metal is used for a ground plane and the transmission lines are formed from second metal. The line-to-line crosstalk of the differential and single-ended transmission lines are summarized in Fig. 4 (dashed lines), with the measured results from the previous section (solid lines) included for comparison.

Simulations of the crosstalk between these structures are not feasible with MDS due to the extremely thin dielectric layer (15 KÅ) between the signal conductors and the ground plane, which leads to a large width-to-height ratio ($\mathrm{W/H} = 13.33$) [7]. These structures are also difficult to simulate with electromagnetic simulators like Momentum. The thin dielectric layer, finite metal conductivity, and the required numerical dynamic range (more than 100 dB) results in impractical computation time and memory requirements. Thus, even with a simple structure, crosstalk simulations can be difficult to obtain. In this case, direct measurement of crosstalk allows quantization of crosstalk.

With a metal ground plane, the crosstalk of all transmission lines is reduced. When compared to structures without ground planes, the differential-mode crosstalk is reduced by at least 20 dB, the common-mode crosstalk is reduced by at least 30 dB, and the single-ended crosstalk is reduced by at least 40 dB. This reduction is a result of the small height of the signal conductors over the ground plane. In this case, the metal ground plane confines electromagnetic fields, causing significantly less coupling (crosstalk) compared to the same structures without the ground plane. The reason for fluctuations of the crosstalk is unclear, but may be related to second-order effects.

V. Conclusions

With the PMVNA and mixed-mode s-parameters, the crosstalk between integrated differential transmission lines can be directly measured. The measured differential-mode crosstalk compared well

with simulated data, providing validation of the measurements. These simple transmission-line structures have illustrated the difficulty in accurately simulating IC crosstalk. Thus, direct measurement of RF crosstalk can be a reliable tool for complicated structures where simulation is not practical or possible. Additionally, these results can be used to estimate the crosstalk between transmission lines of any length less than a quarter-wavelength since the coupling approximately scales with length in this case.

For IC interconnects, several basic conclusions can be supported experimentally. First, differential interconnections on IC's can significantly reduce crosstalk compared to single-ended interconnections. Second, the crosstalk is approximately inversely proportional to the cube of the separation for pairs of differential lines, and inversely proportional to the separation for pairs of single-ended lines. Third, the use of metal ground planes for IC interconnections greatly reduces crosstalk over structures without ground planes. Using differential transmission lines with ground planes, a very high degree of circuit-to-circuit isolation can be achieved, even on high-density IC's.

REFERENCES

[1] D. E. Bockelman and W. R. Eisenstadt, "Pure-mode network analyzer for on-wafer measurements of mixed-mode s-parameters of differential circuits," *IEEE Trans. Microwave Theory Tech.*, vol. 45, pp. 1071–1077, July 1997.

[2] ——, "Combined differential and common mode scattering parameters: Theory and simulation," *IEEE Trans. Microwave Theory Tech.*, vol. 43, pp. 1530–1539, July 1995.

[3] ——, "Calibration and verification of the pure-mode vector network analyzer," *IEEE Trans. Microwave Theory Tech.*, vol. 46, pp. 1009–1012, July 1998.

[4] D. E. Bockelman, W. R. Eisenstadt, and R. Stengel, "Accuracy estimation of mixed-mode scattering parameter measurements," *IEEE Trans. Microwave Theory Tech*, vol. 47, pp. 102–105, Jan. 1999.

[5] D. E. Bockelman, "The theory, measurement, and application of mode specific scattering parameters with multiple modes of propagation," Ph.D. dissertation, Univ. Florida, Dept. Elect. Computer Eng., Gainesville, FL, 1997.

[6] W. R. Eisenstadt and D. E. Bockelman, "Differential and common-mode crosstalk characterization on a silicon substrate," *IEEE Microwave Guided Wave Lett.*, vol. 9, pp. 25–27, Jan. 1999.

[7] Hewlett-Packard Company, Santa Rosa, CA, HP 85150B microwave and RF design syst. user doc., 1992.

[8] R. Lowther, P. A. Begley, G. Bajor, A. Rivoli, and W. R. Eisenstadt, "Substrate parasitics and dual-resistivity substrates," *IEEE Trans. Microwave Theory Tech*, vol. 44, pp. 1170–1174, July 1996.

[9] T. M. Hyltin, "Microstrip transmission on semiconductor dielectrics," *IEEE Trans. Microwave Theory Tech*, vol. MTT-13, pp. 777–780, Nov. 1965.

[10] *HP Momentum A.02: User's Guide*, 3rd ed., Hewlett-Packard Company, Santa Rosa, CA, 1995.

Two-Dimensional Computer Analysis of a Microwave Flat Antenna Array for Breast Cancer Tomography

Alexandre E. Souvorov, Alexander E. Bulyshev, Serguei Y. Semenov, Robert H. Svenson, and George P. Tatsis

***Abstract*—In this paper, we report a two-dimensional computer simulation of a microwave flat antenna array for breast cancer tomography. This new technology promises reduction of X-ray exposure and easier access to peripheral areas of the breast. Using our version of the Newton algorithm, we studied two simple mathematical objects and a more sophisticated two-dimensional model of the breast that takes into account dielectrical properties of different human tissues and malignant tumors. Our calculations show that, operating at 2 GHz, this device may give very reasonable images of tissues located up to 3–4 cm beneath the surface.**

***Index Terms*—Breast cancer, image reconstruction, inverse problems, microwave imaging, Newton method, tomography, tumors.**

I. INTRODUCTION

Microwave imaging of biological objects has been studied for quite a long time. Several prototypes of microwave tomographes have been constructed, and have produced images of a heart, kidney, forearm, and other biological objects [1]–[5]. Recently, it was suggested [6] that microwave imaging may be very promising for breast cancer detection. Using dielectrical properties of breast tissues found in the literature, a finite-difference time-domain (FDTD) simulation of an electromagnetic pulse propagation carried out in [6] showed that backscattered radiation from a cancer tumor as small as 2 mm in diameter is detectable. Provided that it gives clear enough images of the breast tissues, the flat antenna array discussed in [6] would be a great tool. It would eliminate the uncomfortable pressure and exposure to X-rays experienced in mammography. In addition, it can be easily applied to the peripheral areas of the breast, which are hardly accessible by conventional mammography.

Mathematical methods of monofrequency microwave imaging have been discussed extensively in the literature. Different modifications of Born and Rytov approximation methods have been used for problems with relatively low contrast in dielectric properties. More complicated mathematical reconstruction algorithms based on Newton and gradient minimization methods have been developed and successfully used for reconstruction of objects with high contrast. An extensive list of works on this subject can be found in [7]. All of these methods assume that: 1) the scan configuration provides the full view data, i.e., the object is illuminated from all possible directions and 2) the object is embedded in a known and uniform background medium. None of these assumptions is valid for breast imaging with a flat antenna array. For the points that are close to the array, the field of view is about 180°, which is only half of the full view, and it tends to become zero for the points far from the array. This turns the imaging into a limited view problem [8] and will affect its quality. We have every reason to believe that this effect, as well as the absorption, will reduce the visible area to a nearby vicinity of the array. Furthermore, although a breast itself can be considered as a relatively homogeneous medium [6], there are muscles, ribs, and lungs

Manuscript received June 2, 1999. This work was supported by the Carolinas Health-Care System Foundation, Carolinas Medical Center, and Carolinas Heart Institute under a grant.

The authors are with the Laser and Applied Technologies Laboratory, Carolinas Medical Center, Charlotte, NC 28203 USA (e-mail: asouvorov@carolinas.org).

Publisher Item Identifier S 0018-9480(00)06545-5.

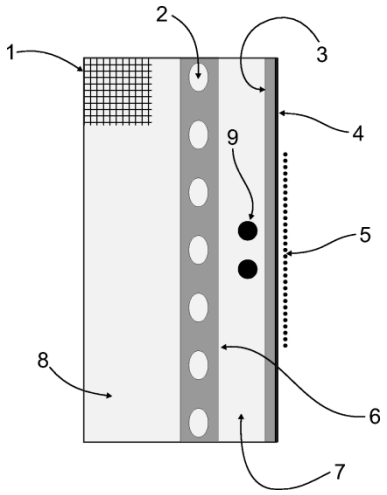

Fig. 1. Geometrical configuration of the calculations and breast model. 1) Part of the mesh for the inverse problem. 2) Ribs. 3) Fat layer. 4) Skin. 5) Antenna array. 6) Muscle layer. 7) Breast tissue layer. 8) Lung layer. 9) Tumors.

only a few centimeters below. However, we hope that the absorption and limited view would restrict the effect of this area on the image.

Located in close proximity of the array, a thin, but high contrast skin layer may produce strong backscattering, which makes the problem even more complicated. We suggest an approximation method of dealing with such a layer, provided that its thickness is sufficiently small.

In this paper, using a modification of the published earlier Newton algorithm [7], we analyze a simplified two-dimensional mathematical model and, in computer experiments, show the possibilities and limitations of breast cancer detection with a flat antenna array.

II. Methods

We examined an ideal model of a two-dimensional 10-cm-wide antenna array of 31 equally spaced elements serving as point-source transmitters and receivers of 2-GHz microwave radiation. This array is located 0.5 cm apart from the breast surface, as shown in Fig. 1 as small black circles. In Figs. 2–4, it has coordinates $x = 0.5$ and $-5 < y < 5$. We suppose that the array is embedded in an immersion medium with the relative permittivity $\varepsilon_0 = 10 - j2$, which is close to that of normal breast and fat tissues [6].

Our study is a computer simulation, which means that, as the first step, we obtain initial data. Using a *mathematical model* of an object, we calculate the fields, which could have been measured by the array in the presence of this object. Then, as if these data were experimental ones, we obtain the image and, finally, compare this image with the original mathematical model.

In the two-dimensional approach, the use of a TM wave has been commonly accepted as a method of reducing the vector Maxwell's equations to the scalar Helmholtz equation. We have earlier described our version of the Newton method for microwave imaging [7]. According to this method, we start with some reasonable guess about the relative permittivity (usually for this purpose we use the permittivity of the immersion medium) and calculate the fields on the array. For this stage, called the direct problem solution, we use the algorithm described in [7] and [9]. Comparing calculated fields with measured ones, we can then improve our guess and, hopefully, obtain a better approximation to the permittivity. This stage is called the inverse problem solution. Repeating these stages, we eventually obtain the final image. We apply the dual-mesh approach [10] when the direct and inverse problems are solved using separate meshes. For the inverse problem, we

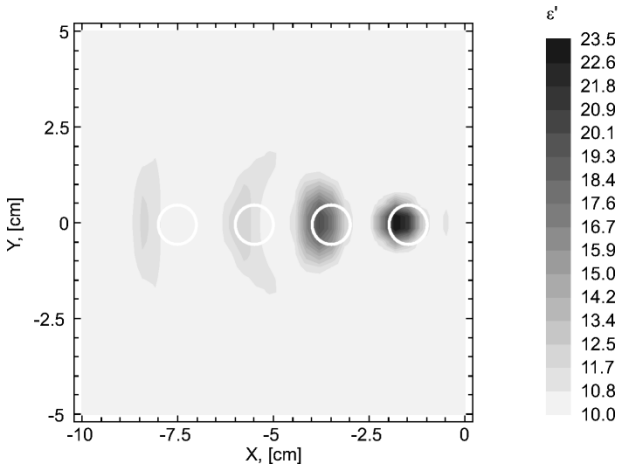

Fig. 2. Reconstruction of four circles plunged on different depths.

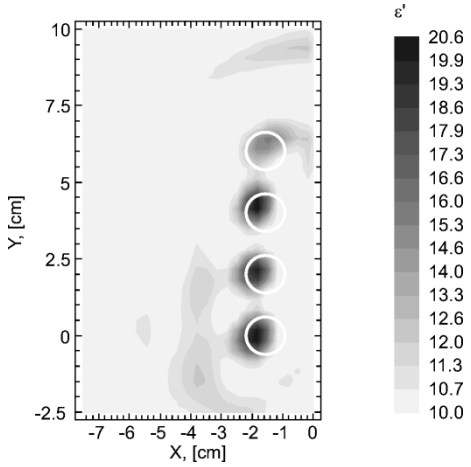

Fig. 3. Reconstruction of a chain of four circles parallel to the array.

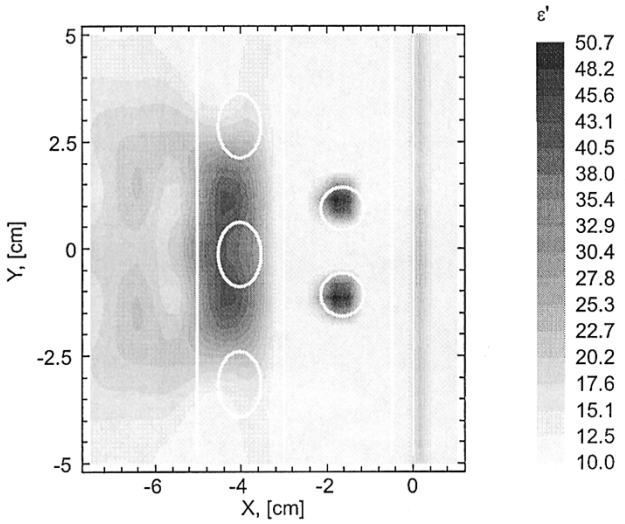

Fig. 4. Reconstruction of the breast model.

use a rectangular mesh, which is half a square 20-cm high and 10-cm wide with 60×30 cells (part of it is shown in Fig. 1). This mesh is embedded into a bigger polar mesh, which is used for the direct problem. The polar mesh is 30 cm in diameter and, usually, has 256 nodes over the angle and 128 nodes over the radius. When we calculate initial data for the objects with a skin layer, we use a very dense mesh of 2048

and 600 nodes. With the receivers being inside the calculational domain, the only modification of our algorithm [7] is the elimination of the last step of the scattered field calculations, which takes into account the wave propagation from the calculational domain to the receivers [7, eq. (13)].

A millimeter-scale thickness of the skin layer presents a considerable challenge for both obtaining the initial data and imaging. In the former case, when we know the exact distribution of the permittivity, we choose a dense enough mesh and solve the problem applying raw computer power. In the latter case, the problem is of a more fundamental nature because the restricted spatial resolution, inherent in the microwave tomography, does not allow us to recover the transverse structure of the skin layer. Although, we can altogether forget about its structure and consider the skin as an infinitesimally thin layer, if the layer is optically thin, which means that its relative permittivity ε_s and thickness h_s meet the condition

$$|2\pi\sqrt{\varepsilon_s}\,h_s/\lambda| \ll 1 \tag{1}$$

where λ is the wavelength in the vacuum. Indeed, the scattered wave E_s induced by the skin layer embedded into the immersion medium with relative permittivity ε_0 can be calculated using the field inside the layer E and Green's function of the Helmholtz equation $G = -\exp(-j\sqrt{\varepsilon_0}\,r/\lambda)/4\pi$

$$E_s = \left(\frac{2\pi}{\lambda}\right)^2 \int (\varepsilon_s - \varepsilon_0) E G\, dV. \tag{2}$$

If condition (1) is met, we can factor out both E and G from the integral over the transverse direction x, which is equivalent to substitution of ε_s for the $\varepsilon_0 + S(y)\delta(x)$, where $S(y) = \int(\varepsilon_s - \varepsilon_0)\,dx$. In terms of the direct problem for the Helmholtz equation, this substitution eliminates the need for any extremely dense mesh and fits nicely into the algorithm described in [7]. In terms of the inverse problem solution, we have to incorporate a new set of unknowns $S(y)$ into the Newton algorithm. This is done in much the same way as described in [7], with the only difference that for $S(y)$ we use the regularization operator $\Delta^{-1}d^2/dy^2$, where Δ is the cell size in Fig. 1. We use the same regularization parameter as for the rest of unknowns (for more details about the regularization see [7]). Providing the algorithm with *a priori* information about the exact position of the infinitesimally thin skin layer, this approach leaves the spatial resolution problem out of consideration. Unfortunately, it is impossible to recover separately the permittivity and thickness of the skin layer, which is an obvious drawback of the method.

We studied three types of objects. First, a chain of four circles 1 cm in diameter and 2 cm apart was aligned across the array. The first circle was placed 1.5 cm from the array. The circles had the relative permittivity $\varepsilon = 25 - j15$. Second, the same chain was aligned with the array. These two objects were used to estimate the visible area.

For the third object, which is a layered model of the breast area shown in Fig. 1, we used dielectric properties of the breast tissue tabulated in [6] and dielectric properties of the other human tissues tabulated in [11]. The model comprised a 5-cm-thick layer of the lung tissue with relative permittivity $\varepsilon_l = 20.8 - j6.1$, a 2-cm-thick layer of the muscle tissue with $\varepsilon_m = 53 - j13$, a 2.5-cm-thick layer of the breast tissue with $\varepsilon_b = 10 - j1.6$, and a 0.5-cm —thick fat layer with $\varepsilon_f = 11 - j1.9$. Simulating ribs, we embedded in the middle of the muscle layer seven ellipses 3 cm apart from each other. The "ribs" were 1.5-cm high and 1-cm wide with $\varepsilon_r = 11.6 - j2.8$. As a model of the cancer tumor, we used two circles 1 cm in diameter and 2 cm apart located 1.5 cm from the surface. We assumed that the permittivity of the malignant area was equal to that of the muscle tissue [6]. On the surface was a 0.1-cm-thick skin layer with relative permittivity $\varepsilon_s = 38.5 - j11.4$. It is worth mentioning that the criterion (1) in this case is about 0.25.

III. Numerical Results and Discussion

Fig. 2 displays the image of the first object. Although slightly deformed, two circles closest to the array are clearly shown. We see only a shadow of the third circle and nothing of the last one. This result restricts the depth of penetration for such a device to 3–4 cm. Similarly, Fig. 3 illustrates that the visible area of a flat array does not extend far beyond its boundaries, which we could have expected from the very beginning.

The image of the breast model is shown in Fig. 4. For the purpose of illustration, *after* obtaining the image, we filled a row of the surface cells with the relative permittivity $\varepsilon_0 + S(y)/\Delta$, where Δ is the mesh size. Close to the array structures, including the malignant zone and skin, are clearly visible. We do not see any trace of the fat layer because it has the permittivity practically equal to that of the normal breast tissue. Structures buried deeper are represented only by vague shapes, at best, allowing for estimation of the thickness of the muscle layer. We can conclude that, although a flat array cannot see clearly deeper than a few centimeters, this does not considerably affect the image of the nearest and most interesting zone. Structures located deeper than 3–4 cm beneath the surface neither appear on the image nor affect the imaging of the upper layers.

We have carried out calculations with different numbers of antennas and different sizes of the mesh for the inverse problem. Reducing the antenna number to 15 does not affect the image quality, while seven antennas seem to be insufficient. The optimal mesh should be twice as wide as the array. Although the array cannot image objects located that far, a smaller mesh tends to distort images.

References

[1] L. E. Larsen and L. H. Jacobi, Eds., *Medical Applications of Microwave Imaging*, NY: IEEE Press, 1986.

[2] J. C. Bolomey and M. S. Hawley, *Methods of Hyperthermia Control*. Berlin, Germany: Springer-Verlag, 1990, ch. 2.

[3] M. Miyakawa and J. Bolomey, Eds., *Non-Invasive Thermometry of the Human Body*. Boca Raton, FL: CRC Press, 1996.

[4] S. Y. Semenov, R. H. Svenson, A. E. Bulyshev, A. E. Souvorov, V. Y. Borisov, Y. E. Sizov, A. N. Starostin, K. R. Dezern, G. P. Tatsis, and V. Y. Baranov, "Microwave tomography: Two-dimensional system for biological imaging," *IEEE Trans. Biomed. Eng.*, vol. 43, pp. 869–877, Sept. 1996.

[5] P. M. Meaney, K. D. Paulsen, A. Hartov, and R. K. Crane, "An active microwave imaging system for reconstruction of 2-D electrical property distributions," *IEEE Trans. Biomed. Eng.*, vol. 42, pp. 1017–1026, Oct. 1995.

[6] S. C. Hagness, A. Tafflove, and J. E. Bridges, "Two-dimensional FDTD analysis of a pulsed microwave confocal system for breast cancer detection: Fixed-focus and antenna-array sensors," *IEEE Trans. Biomed. Eng.*, vol. 28, pp. 1470–1479, Dec. 1998.

[7] A. E. Souvorov, A. E. Bulyshev, S. Y. Semenov, R. H. Svenson, A. G. Nazarov, Y. E. Sizov, and G. P. Tatsis, "Microwave tomography: A two-dimensional Newton iterative scheme," *IEEE Trans. Microwave Theory Tech.*, vol. 46, pp. 1654–1659, Nov. 1998.

[8] A. J. Devaney, "Current research topics in diffraction tomography," in *Inverse Problems in Scattering and Imaging*, M. Bertero and E. R. Pike, Eds. New York: Adam Hilger, 1992, pp. 47–58.

[9] S. Y. Semenov, A. E. Bulyshev, A. E. Souvorov, R. H. Svenson, Y. E. Sizov, V. Y. Borisov, V. G. Posukh, I. M. Kozlov, and G. P. Tatsis, "Microwave tomography: Theoretical and experimental investigation of the iteration reconstruction algorithm," *IEEE Trans. Microwave Theory Tech.*, vol. 46, pp. 133–141, Feb. 1998.

[10] K. D. Paulsen, P. M. Meaney, M. J. Moskowitz, and J. Sullivan, "A dual mesh scheme for finite element based reconstruction algorithms," *IEEE Trans. Med. Imag.*, vol. 14, pp. 504–514, Mar. 1995.

[11] S. Gabriel, R. W. Lau, and C. Gabriel, "The dielectric properties of biological tissues: III—Parametric models for the dielectric spectrum of tissues," *Phys. Med. Biol.*, vol. 41, no. 11, pp. 2271–2293, 1996.

A 140–170-GHz Low-Noise Uniplanar Subharmonic Schottky Receiver

Gildas P. Gauthier, Jean-Pierre Raskin, and Gabriel M. Rebeiz

***Abstract*—A 150-GHz Schottky-diode subharmonic receiver based on a coplanar-waveguide-fed double-folded-slot (DFS) antenna is presented in this paper. The DFS antenna is placed on an extended hemispherical high-resistivity silicon substrate lens to achieve a high directivity and a high coupling to a Gaussian beam efficiency. The uniplanar receiver results in a 12±0.5-dB measured double–sideband conversion loss at 144–152 GHz for a 8–10 mW local-oscillator power at 77 GHz, and has a wide-band ≤13-dB conversion loss over 30 GHz of bandwidth (140–170 GHz). The measured conversion loss includes silicon lens absorption and reflection losses, as well as IF mismatch losses. The applications are in new small aperture (7.5-cm lenses) collision-avoidance radars at 150 GHz.**

***Index Terms*—Millimeter-wave antenna, millimeter-wave receivers, Schottky diode mixers.**

I. Introduction

Automotive electronic applications require light, small, and low-cost circuits at millimeter-wave frequencies. The current design frequency for automotive systems is 77 GHz in Europe and other countries (such as the USA). The far-field beamwidth of an antenna is given by the aperture size and is proportional to λ/D, where D is the aperture diameter. Therefore, at this frequency, 15-cm lenses are required to achieve the appropriate resolution at 100 m (1.5° 3-dB beamwidth). If 154 GHz is used, then the same beamwidth can be achieved using a 7.5-cm lens (Fig. 1). This would make the automotive radar smaller and more practical for modern automobiles.

Integrated-circuit uniplanar receivers consisting of planar antennas, matching networks, and mixers often rely on coplanar waveguide (CPW) technology and offer many advantages over waveguide-based systems. The designs are low cost and easy to fabricate, especially at millimeter-wave frequencies. Two planar CPW-fed antennas have been used commonly in integrated millimeter-wave receivers. The double-slot antenna has been demonstrated in a 94-GHz fundamental Schottky receiver [1], but the antenna geometry does not allow for RF amplification before down conversion. The slot-ring antenna has been used in a W-band integrated monopulse radar receiver based on a subharmonic mixer [2], and is an attractive candidate for array applications due to its compact size. However, the slot-ring antenna has a relatively high input impedance (100–120 Ω) and is not suitable for low-impedance Schottky-diode receivers. In this paper, a 150-GHz uniplanar subharmonic Schottky-diode receiver is developed relying on the double-folded-slot (DFS) antenna, which has a low input impedance [3], [4]. The design follows earlier work done by Raman *et al.* [5], but in an integrated antenna–mixer structure [6], [7]. This is different than waveguide-based subharmonic mixers, which provide excellent performances up to 600 GHz [8], [9]. In this case, the local oscillator (LO) is injected on-wafer, resulting in a simple and compact receiver. The design is compatible with monolithic integration of state-of-the-art Schottky diodes and high-speed transistors for millimeter automotive systems.

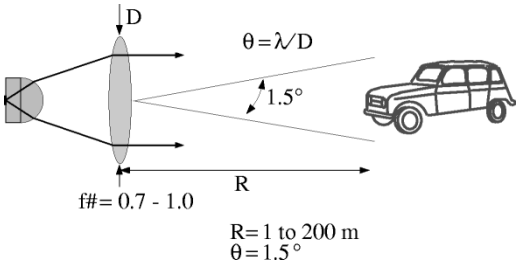

Fig. 1. Radar for automotive applications: 3-dB beamwidth of 1.5° is required to resolve a car at 100 m.

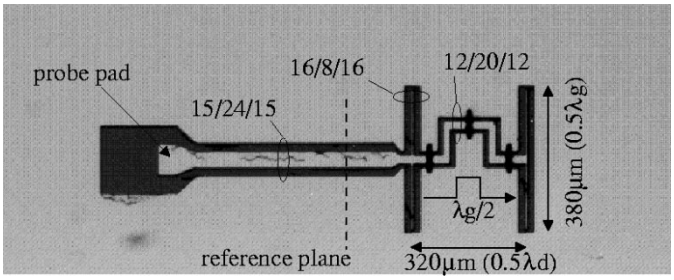

Fig. 2. 150-GHz DFS antenna.

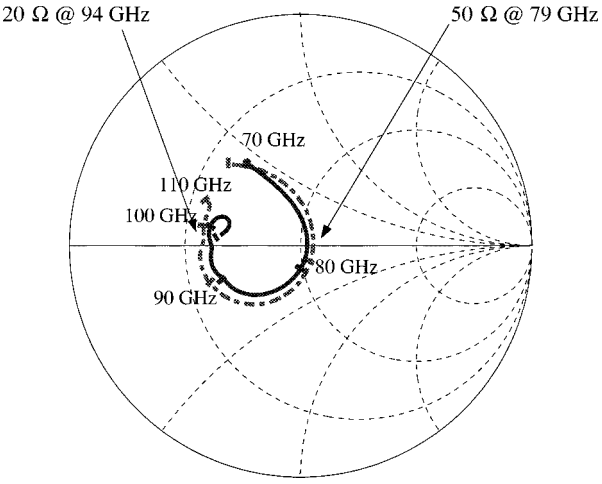

Fig. 3. Measured input impedance of the scaled 70–110-GHz DFS antenna. The input impedance is 20 Ω at 94 GHz.

II. Receiver Design

A. Diode

The subharmonic receiver is based on the University of Virginia Schottky diode SC1T7-D20 and consists of two back-to-back diode junctions with very low junction and parasitic capacitances ($C_{j0} = 2.5$ fF, $C_p = 11$ fF). The dc parameters are deduced by curve fitting from the measured IV curve and are $R_s = 6.5\ \Omega$, $n = 1.163$, $\Phi_b = 0.842$, $\gamma = 0.5$, and $I_0 = 4 \times 10^{-14}$ A, resulting in a figure-of-merit cutoff frequency of $f_c = 1/2\pi R_s(C_{j0} + C_p) = 1.8$ THz. The RF, LO, and IF input impedances of the back-to-back diodes are simulated using an adapted version of Kerr's subharmonic mixer analysis[1] and

Manuscript received July 8, 1999. This work was supported by the Daimler–Benz AG Research Center, Ulm, Germany.

G. P. Gauthier and G. M. Rebeiz are with the Electrical Engineering and Computer Science Department, The University of Michigan at Ann Arbor, Ann Arbor, MI 48109-2122 USA.

J.-P. Raskin is with the Microwave Laboratory, Universite catholique de Louvain, B-1348 Louvain-la-Neuve, Belgium.

Publisher Item Identifier S 0018-9480(00)06544-3.

[1]S. A. Mass, Private Consultant, Diode Mixer Analysis Program, Long Beach, CA, 1997.

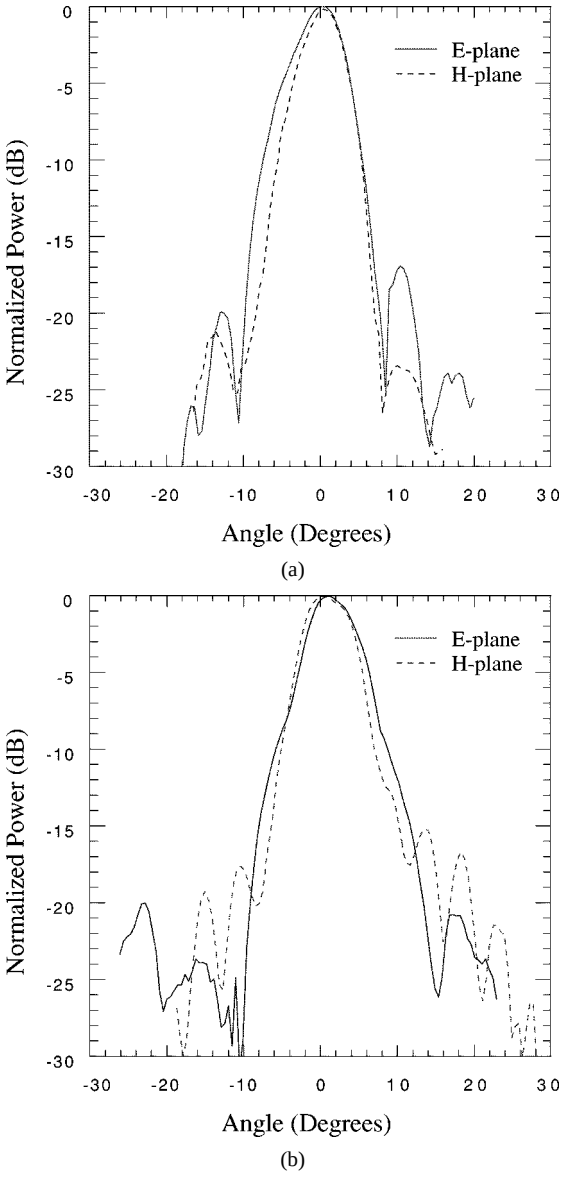

Fig. 4. DFS antenna radiation patterns measured on a 12.7-mm silicon lens at: (a) 150 GHz and (b) 154 GHz. The measured cross-polarization levels in the E- and H-planes are below -25 dB.

are $Z_{\rm RF} = 22 - j30\ \Omega$, $Z_{\rm LO} = 37 - j100\ \Omega$, and $Z_{\rm IF} = 120\ \Omega$ at an RF of 154.2 GHz, an LO of 77 GHz, and an IF of 0.2 GHz, respectively. The minimum double-sideband (DSB) conversion loss for such a diode is simulated to be 5.5–6.0 dB at a 8–10-mW LO power over the 150–154-GHz range. However, with $R_s = 6.5\ \Omega$ due to the skin resistance, the diode series resistance is expected to be around 10–12 Ω at 150 GHz, resulting in a DSB conversion loss of 7–8 dB.

B. DFS Antenna

The DFS antenna is an array of two folded-slot antennas (Fig. 2) placed approximately ($\lambda_d/2$) apart. Each folded-slot antenna acts like a $\lambda_g/2$-long folded CPW line. The wavelengths λ_d and λ_g are the dielectric and guided wavelengths, respectively. The two folded-slot antennas are fed in phase using a $\lambda_g/2$-long (180°-long) CPW line, resulting in symmetrical radiation patterns in the broadside direction, and low cross-polarization levels (≤ -23 dB) [3], [4]. However, the physical separation is ($\lambda_d/2$) for good radiation patterns in the dielectric and is, therefore, shorter than the $\lambda_g/2$ feed line. This problem is easily solved by bending the $\lambda_g/2$ feed line, as shown in Fig. 2.

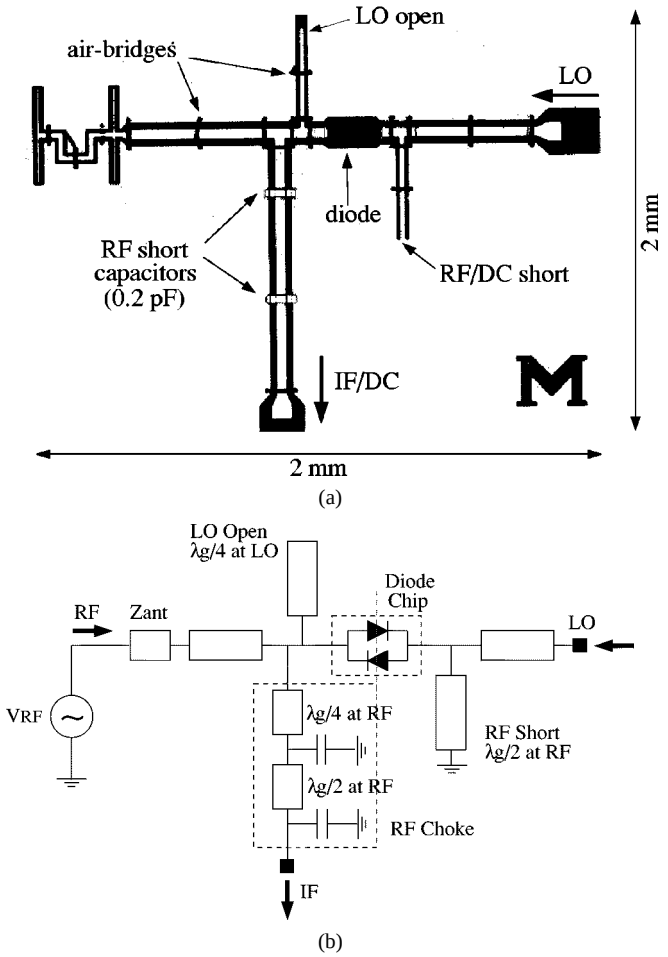

Fig. 5. Layout of: (a) the subharmonic mixer and (b) impedance environment.

The 150-GHz double-folded slot antenna is 380-μm long ($0.5\lambda_g$ or 180° at 154 GHz), with a separation of 320 μm ($0.4\lambda_g$), based on HP Momentum[2] simulations. The input impedance of the DFS antenna has been measured on a scaled version of the antenna at 70–110 GHz and compared with Momentum simulations (Fig. 3). The results indicate that the DFS antenna has a very wide impedance bandwidth with a relatively low input impedance of 20 Ω at 94 GHz (corresponding to 154 GHz), which is a very good match to the diode RF impedance ($22 - j30\ \Omega$). Furthermore, the DFS antenna is a dc open circuit, and no dc filter is needed in the RF port to block the dc-bias component of the diode.

The far-field radiation patterns of the DFS antenna placed nearly at the elliptical position of a 12.7-mm-diameter silicon lens are measured at 150–154 GHz. The measured E- and H-plane patterns at 150 and 154 GHz are shown in Fig. 4. The patterns are symmetrical even with the presence of small amounts of spurious radiation down to the -17-dB level, attributed to the CPW feed line and CPW stubs in the RF circuit. The -3- and -10-dB beamwidths are 8° and 15° at 154 GHz, resulting in a co-polarized directivity of ± 0.2 dB, calculated by averaging the measured E- and H-plane patterns, and a maximum aperture efficiency of 92±3%. The sidelobe levels remain below -15 dB at 150–154 GHz and the measured cross-polarization levels in the E- and H-planes are below -25 dB. The 10-dB beamwidth of 15° is given by the silicon lens (12.7-mm diameter) that was available for pattern measurements; when the DFS antenna is used in a focal plane system, the lens diameter should be reduced to 3.2 mm so as to result in a

[2]HP-EEsof Inc., Westlake Village, CA.

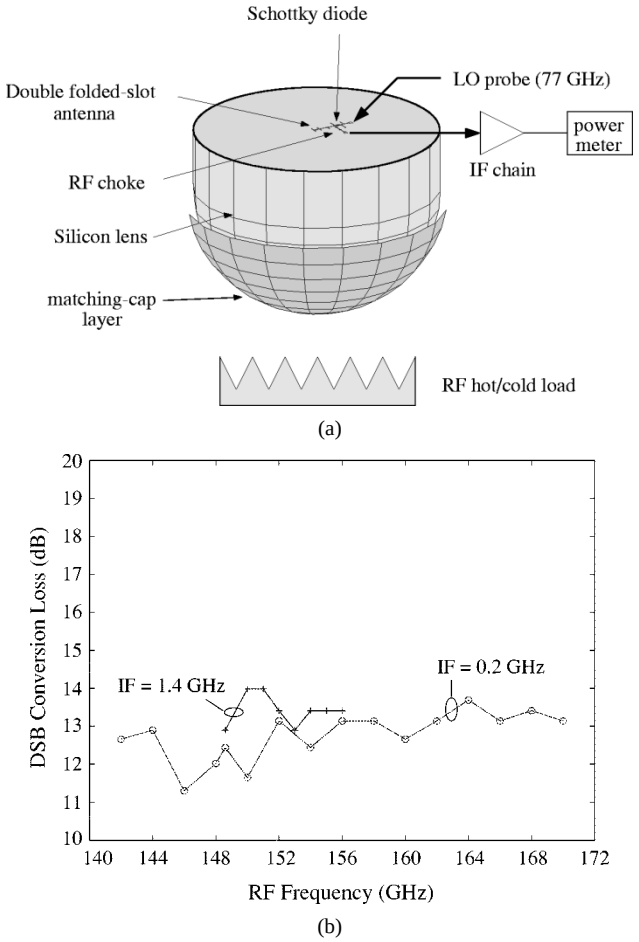

Fig. 6. (a) Measurement setup and (b) measured DSB conversion loss at 142–170 GHz for an IF frequency of 0.2 and 1.4 GHz.

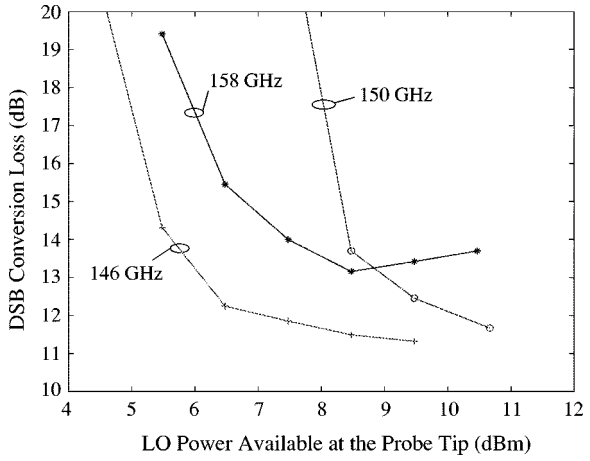

Fig. 7. Measured DSB conversion loss versus LO power available at the probe tip at 146, 150, and 158 GHz.

beamwidth of 60°, which is compatible with f1 lens systems. The diameter of the f1 lens should be around 7.5 cm for a 1.5° beamwidth.

C. Mixer Design

The mixer design is very compact (2 × 2 mm), and LO and RF matching networks are not included for simplicity. The 70–85-GHz LO signal is injected on-wafer with a W-band picoprobe, and is shorted at the RF port by a 417-μm long ($\lambda_{g\mathrm{LO}}/4$) open stub. The RF signal is shorted at the LO port by a 420-μm-long ($\lambda_{g\mathrm{RF}}/2$) shorted stub. The shorted stub also provides the dc and IF shorts. The RF choke consists of two 0.2-pF capacitors placed $\lambda_{g\mathrm{RF}}/2$ apart in the IF port, resulting in a 10-GHz cutoff frequency (Fig. 5). The 0.1–2.0-GHz IF signal is also extracted on-wafer using a K-band probe. The design takes into account the packaged diode feeding lines, which are estimated to be 70° (or 35°) long at the RF (or LO) frequency. The substrate is high-resistivity silicon ($\epsilon_r = 11.7$) capped by 2500 Å of Si_3N_4. The Si_3N_4 layer is etched in the CPW lines, resulting in an effective dielectric constant of $\epsilon_{\mathrm{eff}} = 6.0$ at 77 and 154 GHz. In all cases, the CPW line impedance is 52 Ω ($s = 24$ μm and $w = 15$ μm). The CPW attenuation was measured at 70–110 GHz, and the extrapolated loss at 150 GHz is 0.9 dB/mm.

TABLE I
DETAILED BREAKDOWN OF THE LOSS MECHANISM AND COMPARISON WITH MEASURED RESULTS AT 140–170 GHz

DFS Antenna and Dielectric Lens	
Calculated Back-Side Power Loss	0.5 dB
Estimated Lens Absorption Loss	1.1 dB
Residual Lens-Air Reflection Loss	1.0 dB
DFS Ohmic Loss	~ 1.0 dB
Mixer	
Calculated DSB Diode Conversion Loss	7-8 dB
RF CPW Attenuation Losses	0.8 dB
IF Section	
IF Probe and Atternuation Losses	0.3 dB
Total Calculated DSB Conversion Loss	11.8-12.8 dB
Measured DSB Conversion Loss	12±0.5 dB

III. MILLIMETER-WAVE MEASUREMENTS

The receiver is built using standard photolitographic techniques, and the metallization is 6000 Å of evaporated gold (two skin depths at 150 GHz). The CPW grounds are equalized with electroplated air bridges (20-μm wide, 3-μm thick), and the Schottky diode is connected to the CPW lines using silver epoxy. The receiver is placed on the back side of a 12.7-mm-diameter extended hemispherical silicon lens. The extension length is 2450 μm to reach an intermediate position, where the coupling to a Gaussian beam is 91%. A $\lambda_m/4$-thick stycast matching-cap layer was used to reduce the silicon lens reflection losses [see Fig. 6(a)], where $\lambda_m = \lambda_d/\sqrt{\epsilon_r}$. The IF chain was calibrated at 0.2 and 1.4 GHz, with a gain and noise temperature of 93.8 dB and 110 K, and 93.6 dB and 103 K, respectively.

The subharmonic receiver DSB conversion loss was measured using the hot/cold load method for an IF frequency of 0.2 and 1.4 GHz and are presented in Fig. 6. A receiver DSB conversion loss of 12±0.5 dB is measured at 144–152 GHz, for an available LO power of 8–10 mW at the probe tip (Fig. 7). The conversion loss is close to values obtained in current 77-GHz radar systems. The conversion loss is less than 13 dB at 140–170 GHz, resulting in a 20% bandwidth. The measurement includes the IF mismatch and probe losses (0.3 dB), the backside radiation losses (calculated to be 0.5 dB), and the silicon lens absorption losses (1.1 dB). Also, the CPW attenuation loss between the antenna and mixer is estimated to be 0.8 dB at 150 GHz. The ripples in the measurements indicate the matching-cap layer is not optimum and the reflection losses at the silicon–air interface are estimated to

be 1.0 dB. The total calculated losses are then 10.7-dB DSB, including the ohmic losses in the DFS antenna, estimated to be 1.0 dB (due to the small dimensions of the folded slots), but not including the losses of the stubs before and after the diodes. This compares well with the measured 12±0.5-dB DSB conversion loss (Table I).

IV. Conclusion

A planar integrated subharmonic receiver has been developed at 140–170 GHz. The receiver shows a wide-band DSB conversion loss of 11.5–13.5 dB at 140–170 GHz due to the wide-band low-input impedance of the antenna (20 Ω), which presents a good match to the subharmonic diode input impedance ($22 - j30$ Ω). The local oscillator can be integrated on-chip at 77 GHz, resulting in a low-cost uniplanar monolithic receiver for future automotive applications.

References

[1] G. P. Gauthier, W. Y. Ali-Ahmad, T. P. Budka, D. F. Filipovic, and G. M. Rebeiz, "A uniplanar 90-GHz Schottky diode millimeter wave receiver," *IEEE Trans. Microwave Theory Tech.*, vol. 43, pp. 1669–1672, July 1995.

[2] S. Raman, S. Barker, and G. M. Rebeiz, "A W-band dielectric-lens-based integrated monopulse radar receiver," in *IEEE MTT-S Int. Microwave Symp. Dig.*, 1998, pp. 517–520.

[3] G. P. Gauthier, S. Raman, and G. M. Rebeiz, "A 90–100 GHz double-folded slot antenna," *IEEE Trans. Antennas Propagat.*, vol. 47, pp. 1120–1122, June 1999.

[4] T. M. Weller, L. P. B. Katehi, and G. M. Rebeiz, "Single and double folded-slot antennas on semi-infinite substrates," *IEEE Trans. Microwave Theory Tech.*, vol. 43, pp. 1423–1428, Dec. 1995.

[5] S. Raman, F. Rucky, and G. M. Rebeiz, "A high-performance W-band uniplanar subharmonic mixer," *IEEE Trans. Microwave Theory Tech.*, vol. 45, pp. 955–962, June 1997.

[6] L. Trong-Huang, C. Chen-Yu, J. R. East, G. M. Rebeiz, and G. I. Haddad, "A quasi-optical subharmonically pumped receiver using separately biased Schottky diode pairs," in *IEEE MTT-S Int. Microwave Symp. Dig.*, vol. 2, 1994, pp. 783–786.

[7] S. Raman, N. S. Barker, and G. M. Rebeiz, "A W-band dielectric-lens-based integrated monopulse radar receiver," *IEEE Trans. Microwave Theory Tech.*, vol. 46, pp. 2308–2316, Dec. 1998.

[8] I. Mehdi, M. Mazed, R. Dengler, A. Pease, M. Natzic, and P. H. Siegel, "Planar GaAs Schottky diodes integrated with quartz substrate circuitry for waveguide subharmonic mixers at 215 GHz," in *IEEE MTT-S Int. Microwave Symp. Dig.*, vol. 2, 1994, pp. 779–782.

[9] I. Mehdi, P. H. Siegel, D. A. Humphrey, T. H. Lee, R. J. Dengler, J. E. Oswald, A. Pease, R. Lin, H. Eisele, R. Zimmermann, and N. Erickson, "An all solid-state 640-GHz subharmonic mixer," in *IEEE MTT-S Int. Microwave Symp. Dig.*, vol. 2, 1998, pp. 403–406.

Reflection Resonances and Natural Oscillations of Two-Aperture Iris in Rectangular Waveguide

Anatoly A. Kirilenko and Lyudmila P. Mospan

***Abstract*—The total reflection resonances that take place at the excitation of a two-slot resonant iris in rectangular waveguide are discussed in this paper. Considering the iris as an open-resonator-waveguide structure, the pair of natural oscillations responsible for such resonances was numerically found and investigated. It is pointed out to a parallel between the rejection resonances in two-slot irises and "locked"-mode resonances in multimode waveguide structures.**

***Index Terms*—Complex natural frequencies, multislot iris, rectangular waveguide, rejection resonance.**

I. Introduction

The multiple rectangular aperture irises have aroused some interest before due to a possibility to design low-cost bandpass filters with low insertion loss and increased spark-over voltage or with some improved stopband attenuation (see, e.g., [1], [2]). Apparently, the ability of multiple-rectangular aperture irises to form a rejection response was for the first time mentioned in [3], where experimental data of a five-aperture iris response were presented. An approximate estimation of a rejection resonance position, based on the circuit theory modeling, was also proposed in [3]. It was suggested that the reason for the resonance might be the additional inductance conditioned by a vertical metal strip that was placed between two pairs of slots of the same width. Later on, in [2], a more detailed investigations of such rejection resonances (with a bandwidth of 10%) and a more accurate electromagnetic estimation of their characteristics were given. As we shall indicate further, total reflection resonances can be found even in the simplest two-aperture irises, and the rejection resonance band can be much narrower.

The aim of this paper is to analyze such resonances in a more detailed manner, to interpret their nature from a novel point-of-view, and to attract the attention to possible applications of two-aperture irises in bandstop filters.

As a tools for investigation, a numerical model based on the mode-matching technique and generalized S-matrix technique were used.

II. Numerical Results and Interpretation

The characteristic curves of the frequency responses of two-aperture irises in the rectangular waveguide excited by the TE_{10} mode are presented in the upper parts of Figs. 1–3. Along the horizontal axes, the values of the real (f) and the normalized $\kappa = 2\pi\omega c^{-1} = a/\lambda_0$ frequencies are plotted. As an example, we refer to the iris of 0.5-mm thickness with two slots of 1-mm widths adjacent to the upper and lower wide walls of the waveguide WR-90 (see insert in Fig. 1). The positions of the apertures along the vertical axis do not have a principal importance and all the below-mentioned regularities are retained. The widths of the apertures change from Fig. 1 to 3 in such a way that $\Delta = (a_2 - a_1)$ varies from 0 to 3 mm with a fixed ratio $(a_1 + a_2)/2 = 14.5$ mm. Evidently, the response shown in Fig. 1 for the case of two similar apertures coincides, by virtue of the symmetry of the structure, with that for the centered single aperture of the double height in the

Manuscript received April 19, 1999.

The authors are with the Department of Computational Electromagnetics, Institute of Radiophysics and Electronics of the National Academy of Science of Ukraine, Kharkov 310085, Ukraine (e-mail: kirilenko@ire.kharkov.ua).

Publisher Item Identifier S 0018-9480(00)06543-1.

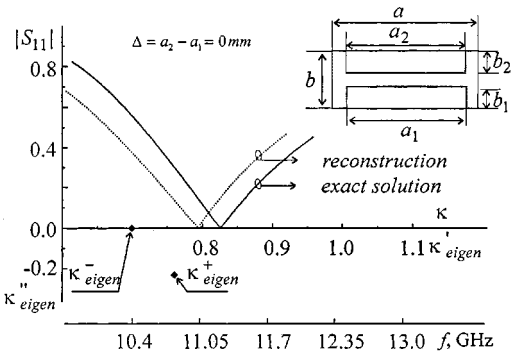

Fig. 1. Frequency response of the two-slot iris for zero difference between the widths of the upper and lower slots. The solid curve is the exact solution of the scattering problem. The dashed curve is the frequency response reconstruction in accordance with two natural frequencies. In the lower part of the figure, the locations of two complex natural frequencies are marked for "symmetrical" and "antisymmetrical" oscillations.

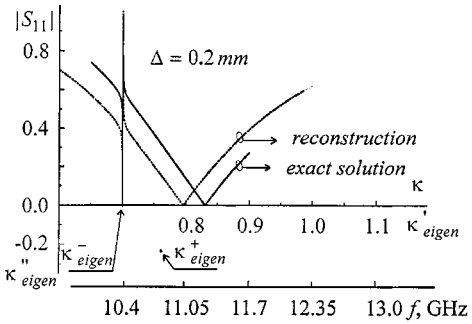

Fig. 2. Frequency response of the two-slot iris for a small difference between the widths of the upper and lower slots.

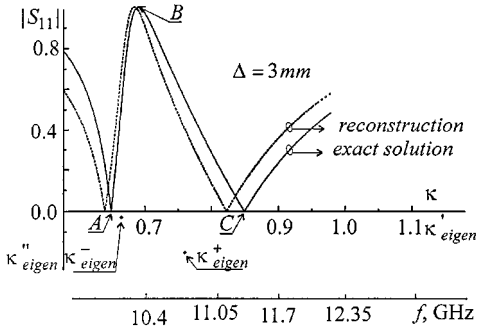

Fig. 3. Frequency response of the two-slot iris for a large difference between the widths of the upper and lower slots.

same waveguide and is typical for conventional irises used as separate bandpass sections. The characteristic high-Q "resonance–antiresonance" pair appears immediately as soon as two resonant apertures become different (Fig. 2). This resonance pair takes place much lower in frequency than the conventional low-Q resonance of total transmission and the rejection resonance turns out to be located between two points of complete matching. By increasing the difference in the widths of apertures, a newly appeared resonance can be made less sharp: for $\Delta = 3$ mm (Fig. 3), the frequency response looks as an "overlapping" of characteristics of two single-aperture irises. However, there is an essential distinctive property of two-slot iris responses. In contrast to the case of a pair of sequentially placed irises, here we always have a total reflection point between two full matching points. For two very different apertures ($\Delta > 5$ mm), a wide strong-reflection zone appears

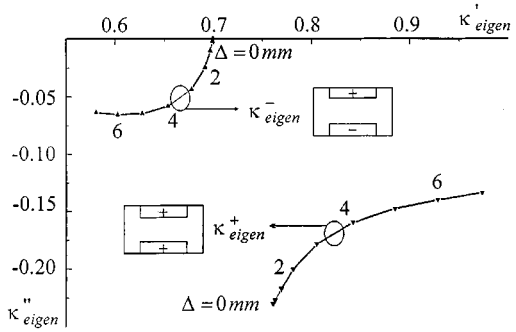

Fig. 4. The natural frequencies of "symmetrical" ($\kappa^-_{\rm eigen}$) and "antisymmetrical" ($\kappa^+_{\rm eigen}$) modes of the two-aperature iris as a function of difference between widths of the upper and lower slots.

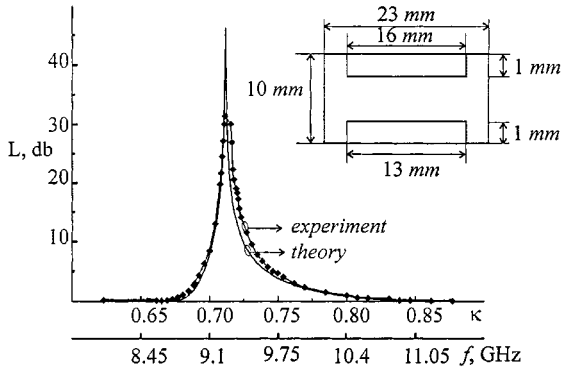

Fig. 5. The measured and simulated frequency responses for the two-slot copper iris of 0.48-mm thickness placed in the WR-90. The slots' dimensions are 13.0 × 1 mm^3 and 16.0 × 1 mm^2.

between points of matching, and it also has a full reflection point corresponding to $|S_{11}| = 1$. The behavior of the amplitudes of the fields that are excited in the iris slots is very interesting. The phases of the slot fields at the first complete transmission point (A) (see Fig. 3) are equal to 180° and 0°, and so the fields are antiphased, but at the second total transmission frequency (C), these phases are equal to 0° and −1° and the fields are almost in phase. At the total reflection point (B), the fields in the slots are antiphased being ±90° shifted in relation to the field of incident mode. The dynamics of the resonance appearance and the character of the field behavior in the slots suggest the excitation of two natural oscillations in a two-aperture iris as an open electromagnetic structure. One of these oscillations has a high-Q factor $\Delta/a \ll 1$ and the antiphase field distribution in the slots, and the other has a low-Q factor and the in-phase fields in the slots. By a Q factor of eigenoscillation of an open structure, we meant here the relation between radiation loss and stored energy, such a Q factor may be numerically estimated as the ration between real and imaginary parts of complex eigenfrequency.

In order to justify such an interpretation, the solutions of a corresponding homogeneous equation in the complex frequency domain were numerically found. For the complex frequency $\kappa_{\rm eigen} = 2\pi\omega^{-1}_{\rm eigen} = \kappa'_{\rm eigen} + i\kappa''_{\rm eigen}$ ($\kappa''_{\rm eigen} < 0$, time dependence $e^{-i\omega t}$), two branches of natural oscillations were found that corresponded to two transmission resonances of a two-aperture iris. These branches are presented in Fig. 4, where the difference of the slot widths Δ is used as a parameter in the curves. We denote these natural frequencies as $\kappa^-_{\rm eigen}$ and $\kappa^+_{\rm eigen}$ in accordance with the eigenoscillation character in the limit $\Delta \to 0$ on the left-hand-side and right-hand-side branches, respectively. The "antisymmetrical" natural oscillation does not have any coupling with the $\rm TE_{10}$ modes

of the output-waveguides that take away the power and, therefore, it is quite natural that on the left-hand-side branch $\kappa''_{\rm eigen} = 0$ if $\Delta = 0$. In this limit, the symmetrical oscillation has a finite and at the same time fairly low-Q factor. It is the excitation of a similar natural oscillation the explains the known resonance in a conventional resonance iris-bandpass section.

For each iris whose responses are shown Figs. 1–3, the values of the corresponding natural frequencies are presented in the lower part of the figures by diamond marks. As usual, the positions of the resonance points are close to the real parts of the complex frequencies only for the high-Q modes with $|\kappa''_{\rm eigen}| \ll \kappa'_{\rm eigen}$, which is visible in Fig. 2. Along with that, the peculiarities of characteristics in all the cases form Figs. 1–3 can be perfectly explained by the excitation of two natural oscillations in the iris. To this end, it will suffice to compare the pairs of solid and dashed curves in these figures. They correspond, respectively, to the full-wave numerical solution of the diffraction problem and to the solution constructed after an approximate formula

$$S^{11}(\kappa) = \frac{1}{2}\left(\frac{(\tau-\tau_+)(\tau+\overline{\tau}_+)(\tau-\tau_-)(\tau+\overline{\tau}_-)}{(\tau-\overline{\tau}_+)(\tau+\tau_+)(\tau-\overline{\tau}_-)(\tau+\tau_-)}+1\right). \quad (1)$$

Here, $\tau = \sqrt{\kappa^2 - 1/4}$, $\tau_{+(-)} = \sqrt{\kappa_{\rm eigen}^{+(-)2} - 1/4}$ and the dash over $\tau^{+(-)}$ denotes the operation of complex conjugation. Equation (1) is a special case of a more general expression derived in [6] as a result of the S-matrix reconstruction for an open waveguide-type resonator in accordance with the set of complex frequencies. Equation (1) describes the response with only two natural oscillations taken into account. As we can see, both exact and approximate solutions are in good qualitative agreement; in terms of the high-Q resonance estimation, they agree even for quantitatively. Measurements for some two-slot irises were performed in order to verify the influence of real ohmic loss and other factors on the possible level of suppression. The measured frequency response for the two-slot copper iris of 0.48-mm thickness placed in a WR-90 waveguide is shown in Fig. 5. The slots of 13.0 $\times$ 1 mm^2 and 16.0 $\times$ 1 mm^2 dimensions were cut near the upper and bottom walls. Insertion loss at the resonance frequency of 9.295 GHz turned out -32 dB. As a comparison, the simulated response is shown in Fig. 5.

III. Conclusion

Thus, shown above, two slots of different widths are enough to provide the existence of the total rejection resonance in the frequency response of the iris in rectangular waveguide. The very existence of such resonances might be interpreted as a response to the excitation of a pair of natural oscillations in the open-waveguide-type structure. Concerning the nature of their appearance, these resonances are close to those on the "locked" modes that are explained (see, e.g., [7]) by the excitation of high-Q natural oscillations formed by the "locked" mode on the background of low-Q resonances that are connected with the dominant mode. Numerical investigation of the possibilities to control the location and the Q factor of the total reflection resonance has shown that, based on these effect, we can design bandstop filters with 2%–10% bands and satisfactory insertion losses in the passband.

References

[1] W. Hauth, R. Keller, U. Papziner, R. Ihmels, T. Sieverding, and F. Arndt, "Rigorous CAD of multiport coupled, rectangular waveguide component," in *Proc. 23rd EuMC'93*, pp. 611–614.

[2] R. Yang and A. S. Omar, "Investigation of multiple rectangular aperture irises in rectangular waveguide using TE$^{\rm x}$ mn modes," *IEEE Trans. Microwave Theory Tech.*, vol. 41, pp. 1369–1373, July 1993.

[3] N. G. Paterson and I. Anderson, "Bandstop iris for rectangular waveguide," *Electron. Lett.*, vol. 12, no. 22, pp. 592–594, 1976.

[4] V. G. Alybin *et al.*, "Double resonance waveguide iris" (in Russian), *Radiotek. Elektron.*, no. 8, pp. 1605–1613, 1981.

[5] H. Parzelt and F. Arndt, "Double-plane steps in rectangular waveguides and their application for transformers, irises, and filters," *IEEE Trans. Microwave Theory Tech.*, vol. MTT-30, pp. 7711–7777, May 1982.

[6] A. A. Kirilenko and B. G. Tysik, "Connection of S-matrix of waveguide and periodical structures with complex frequency spectrum," *Electromagnetics*, vol. 13, no. 3, pp. 301–318, 1993.

[7] A. A. Kirilnko, S. L. Senkevich, and B. G. Tysik, "Features of resonant phenomena in open waveguide structures of waveguide type" (in Russian), *Radiotek. Elektron.*, vol. 35, no. 4, pp. 687–694, 1990.